Università degli Studi di Catania
FACOLTÀ DI INGEGNERIA

DIPARTIMENTO DI INGEGNERIA ELETTRICA ELETTRONICA E DEI SISTEMI

TESI DI DOTTORATO DI RICERCA IN INGEGNERIA ELETTRONICA, AUTOMATICA E CONTROLLO DI SISTEMI COMPLESSI

XXIII CICLO

ALESSANDRO SPATA

SISTEM: a new method to integrate geodetic and satellite data to estimate 3D ground deformation maps

Coordinator:
Prof. L. Fortuna

Tutor:
Prof. G. Nunnari

Acknowledgements

A sincere thank goes to my tutor Prof. Giuseppe Nunnari who, first, gave me the chance to spread my wings toward research and who always represents for me a sample of scientific rigor and devotion.

I would like to express my gratitude to Dr. Giuseppe Puglisi for giving me the opportunity to work in the interesting area of Volcano Geophysics and for his guidance, support, and advice throughout these studies.

I am indebted to “Istituto Nazionale di Geofisica e Vulcanologia” for providing the financial support throughout the Ph.D.

I am grateful to the members of the research groups of the “Unità Funzionale Deformazioni del Suolo” at INGV for their support; especially to Dr. Francesco Guglielmino and Dr. Alessandro Bonforte for their useful assistance. I am grateful to other members of the INGV of Catania, Eng. Michele Prestifilippo, Eng. Gaetano Spata, Eng. Flavio Cannavò, Eng. Dino Montalto. Whenever I had problems in my research they was always there to help me.

I would like to thank my family, my parents, and my brothers to be always ready to encourage me.

A very special thanks to Rita Cambria Zurro Rapisarda, my girlfriend.

Index

Introduction

The aim of this work is to propose a new method in order to efficiently produce high-resolution maps relevant to the three-dimensional motion of Earth's surface by combining information from sparse Global Position System (GPS) measurements and Differential Interferometric Synthetic Aperture Radar (DInSAR) data.

The use of DInSAR and GPS data to monitor ground deformations on the same active tectonic or volcanic areas are extensively used [1]; Plate Boundary Observatory (PBO) web-pages at UNAVCO http://pboweb.unavco.org/].

Nevertheless, each technique has some significant shortcomings when used in a stand-alone mode. Although GPS is the most suitable technique for measuring ground deformation with sub-cm accuracy level, it provides a point wise 3D displacement vector referring to the specific geodetic benchmark where the antenna is set up; consequently, the spatial resolution of the measurement of the ground deformations depends on the network geometry and thus is usually low (in the order of a few points / km^2, in the optimal conditions). DInSAR provides displacement measured along the Line Of Sight (LOS) between the Earth's surface and the sensor; for satellite systems, which have off-nadir angles of about 20°-40 °, this implies that DInSAR measurements are more sensitive to the vertical component of the deformation than to the horizontal ones. Since the DInSAR measures along a specific direction (LOS), the dimension of the information on the ground deformation is a scalar. The DInSAR surveys provide maps of the Earth's movements having pixel size in the order of 20 m × 20 m; thus the spatial resolution is higher than the GPS network. The accuracy of the DInSAR measurements is in the order of the cm, being the knowledge of the orbits, the accuracy of the DEM and the propagation thought the atmosphere the main sources of errors. Except for the

first two, which can be reduced by adopting specific procedures, the atmosphere (and in particular the troposphere) is at the origin of the main unpredictable perturbing effects. The variations of the troposphere may affect the ground deformation measurements over ten of centimetres in very unfavourable conditions due, for instance, to turbulences on mountainous areas [2]. However, the atmospheric signal follows, on the whole, the power law distribution and in general we may expect effects in the order of 0.5-1 interferometric fringe (e.g. ~ 1.5-3 cm, for a C-band SAR [3,4] [*Bonforte et al.,* 2001, Mattia et al., 2007]. Several techniques have been proposed during the last decade to reduce or eliminate the tropospheric effects on DInSAR data [5, 6, 7], but none of these can be considered as definitive and each of these has pro or cons depending on the specific experimental conditions. .

The integration of DInSAR (scalar) data with the GPS (vector) data should provide information on the ground deformations by taking advantage of the positive features of both these techniques, i.e. the high spatial resolution of the DInSAR, the 3D measurements and the sub-cm accuracy level of GPS. This integrated information should be able to give a more reliable interpretation of the geophysical phenomena producing ground deformations.

Recently, a few methods aimed at integrating these two kinds of data have been published [8, 9]. Gudmundsonn et al. [8] applied a Bayesian statistical approach and Markov Random Field (MRF) theory to derive 3-D velocity maps, while Samsonov and Tiampo [9] introduced an analytical optimization of interferometric observation and GPS dataset. Apart from the differences in the algorithms used for combining the data, these two methods have two points in common: the first is the preliminary interpolation step in which sparse GPS measurements are interpolated in order to fill in GPS displacements at the DInSAR grid and the second one is that the optimization techniques used to combine the different datasets are not based on the physics of the deformations (i.e. from the elasticity theory).

The interpolation technique typically used in these two methods is the kriging which requires for each component to be interpolated, the choice of an appropriate theoretical semivariogram model. This choice is one of the main critical points in geostatistics [10] and it is usually performed by supervising a preliminary statistic analysis of the experimental data.

Here we propose the SISTEM (Simultaneous and Integrated Strain Tensor Estimation from geodetic and satellite Measurements) method, a Weighted Least Square (WLS) approach totally based on the elastic theory, to simultaneously integrate GPS and DInSAR data without requiring the preliminary step of the GPS interpolation. In this way, the dependence on the choice of the theoretical semivariogram model, required by the kriging interpolator, is avoided. Furthermore, this method computes the results on each point of the Earth's surface and, being based on elastic theory, it provides the 3D strain and the rigid body rotation tensors. The estimated standard errors computed by the WLS for each computation point are also provided to assess the reliability of the results.

Furthermore 3D ground deformation maps, obtained thought the SISTEM method, were used in the framework of the inversion problem. In this context an inversion procedure based on the joined use of a Particle Swarm Algorithm and the Gauss-Newton optimization methods was used to solve the inversion problem relevant to the 2009 Abruzzo earthquake. Moreover, other novelty of this work, a neural network based approach aimed to estimate more realistic volcanic source shape instead of perfect geometric source shape was proposed.

This work is organized as follows. In chapter 1 the state of the art relevant to the integration of geodetic and satellite data to obtain 3D motion maps over the whole investigated area is reported. In particular the methods developed by S. Gudmundsson and F. Sigmundsson [8], *Three-dimensional surface motion maps estimated from combined interferometric synthetic aperture radar and GPS data*, and the method developed by Samsonov and Tiampo [9],

Analytical optimization of InSAR and GPS dataset for derivation of three-dimensional surface motion, are reported. Chapter 2 describes the new method we have developed in order to integrate geodetic and satellite data. Chapter 3 is devoted to the inversion modeling problem. In chapter 4 a new method based on Artificial Neural Network aimed to estimate a more realistic volcanic source shape is proposed. Finally the conclusions of this work are drawn.

Chapter 1

State of the art

The S. Gudmundsson and F. Sigmundsson method

In the following we report the method proposed by S. Gudmundsson and F. Sigmundsson for fusion of InSAR and GPS data to achieve three-dimensional surface motion map. This method uses Markov Random Field (MRF) based regularization and simulated annealing optimization [11, 12]. In MRF regularization, an optimal image is interpreted as a realization of a random variable, where the value of each pixel in the image grid is only dependent on its nearest neighbors. This provides a convenient way of modeling image texture and spatial correlation of image pixels. Furthermore, simulated annealing optimization of MRF regularization is a very suitable and effective method to use in image reconstruction.

This methodology can be used to construct 3-D motion maps of various types of surface movements. Such motion maps can be useful e.g., (1) to display data and provide a consistent view of 3-D motion fields, (2) to derive strain rate maps that can be used to study the buildup of crustal stresses related to future earthquakes, and (3) to infer volume of surface uplift/subsidence by integration of vertical deformation fields.

Problem formulation

An InSAR interferogram can be related to the 3D ground deformation components as

$$V_{LOS}^{i} = \left[v_x^i; v_y^i, v^i{}_z\right]\left[S_x, S_y; S_z\right]^T \qquad (1)$$

where i is a pixel number, $v_x^i, v_y^i \; and \; v^i{}_z$ are the east, north and vertical components of deformation, respectively, and $S = [S_x, S_y; S_z]$ is a unit vector pointing from ground toward satellite. The aim is to estimate the three motion map $v_x, v_y \; and \; v_z$ from the known V_{LOS} interferogram and sparse GPS observation values of $v_x, v_y \; and \; v_z$. The authors rewrite the three-dimensional equation as the two equivalent two-dimensional terms for computational convenience

$$V_{LOS} = [v_L^i, v_V^i][S_L, S_V]^T \tag{2}$$

where

$$S_L = \sqrt{S_E^2 + S_N^2} \tag{3}$$

$$v_L^i = \frac{[v_{x,}^i \, v_{y,}^i][S_x, S_y]^T}{S_L} \tag{4}$$

The second term v_L^i is the deformation in the horizontal look direction of the satellite. Equation (2) can be first used as a basis to determine v_L, v_V. Then the east and north motion maps, v_x, v_y can be found by utilizing equation (4) or by rewriting equation (1) as

$$V_{LOS}^i - S_v v_V = [v_x^i; v_y^i][S_x, S_y]^T \tag{5}$$

The authors adopt the following general formulation of equation (2) and (5):

$$y_1^i = [x_1^i; x_2^i][S_1, S_2]^T \quad (6)$$

where y_1^i is known for all pixel *i*, x_1^i and x_2^i are only known at sparse locations and $S_1 \, and \, S_2$ are constants. By using equation (6), the problem of optimizing three motion maps in equation (1) is simplified to optimization of the two motion map $x_1 \, and \, x_2$. Hence the same optimization algorithm can be used when optimizing $x_1 = V_L$ and $x_2 = V_V$ in equation (2), and $x_1 = V_E$ and $x_2 = V_N$ in equation (5). This simplifies the optimization algorithm, since only two instead of three motion maps are optimized at the same time. This does though require V_L and V_V to be optimized previous to V_E and V_N.

An introduction to the Markov Random Field Regularization and Simulated Annealing Optimization

S. Gudmundsson and F. Sigmundsson use a MRF model to regularize the construction of the x_1 and x_2 motion maps in equation (6). The regularization is optimized with a simulated annealing iteration process. According to the MRF regularization, an optimal image x is interpreted as a realization of a random field X. The authors adopt a maximum a posteriori (MAP) estimate in order to represent an optimal realization image x for a given image y. The MAP estimation is given as

$$\hat{x} = \arg\max_x P(X = x \mid Y = y) \quad (7)$$

For convenience $P(X = x)$ will be written as $P(x)$ when expressing the likelihood. The Bayesian theorem [13] gives

$$P(x \mid y) = \frac{P(x)P(y \mid x)}{P(y)} \propto P(x)P(y \mid x) \tag{8}$$

where $P(x)$ represent prior expectations about the random field X.

A Markov random field X is characterized by the important property that it is defined with respect to its neighborhood system, such that a pixel value on an image grid is assumed to be conditionally dependent on its neighboring pixels only. This is the Markov property, which gives a local definition of the random field. The authors use this property when a simulated annealing is adopted to optimize the MRF regularization, which results in a very effective image optimization process. By using the Hammersley-Clifford theorem [14], the density function in equation (8) can be written as the Gibbs random field

$$P(x \mid y) = P_T(x \mid y) \propto \exp\left(-\frac{1}{T}U(x \mid y)\right) = \exp\left(-\frac{1}{T}U_1(x)\right)\exp\left(-\frac{1}{T}U_2(y \mid x)\right) =$$

$$= \exp\left(-\frac{1}{T}U_1(x) + U_2(y \mid x)\right) \tag{9}$$

where $U(x \mid y)$ is an energy function defined with respect to the neighbourhood structure of the image x, (i.e. $U_1(x)$) and the relationship of the image *x* to the image *y* (i.e. $U_2(x)$), and *T* is a temperature. The Hammersley-Clifford theorem gives a global definition of the random

field, and hence the MRF modeling can be regarded as defining a suitable energy function that takes its minimum energy stage for the optimal realization image.

As $T \to \infty$ the distribution in equation (9) becomes uniform among all possible energy states and as $T \to 0$, the distribution becomes uniform among the minimum energy states. The simulated annealing optimization can be described as a sampling of the density in equation (9), where the temperature *T* starts at some ‘‘high’’ value $T_0 > 0$ and falls toward 0 during the iteration steps. If the temperature is lowered slowly enough, then equation (9) will assign the maximum probability to the MAP image [15]. One of the great advantages of using the simulated annealing optimization process is its relatively low risk of running into a local minimum compared to other optimization algorithms.

Construction Process

The authors start their construction process with initial motion maps created from interpolated GPS observations. The motion maps are then optimized further with MRF regularization and the simulated annealing algorithm.

The initial motion maps are used as initial guesses before optimizing the 3-D motion field with the MRF regularization. Various methods exist for interpolation of sparse data [16]. The effectiveness of each method may depend on the characteristics of the sparse data. A reasonable chose of interpolation method needs to be considered with respect to each sparse data set. The authors demonstrate the method selected to interpolate the sparse data and discuss some other possible alternatives.

In particular S. Gudmundsson and F. Sigmundsson tested several interpolation methods for the sparse GPS data from the Reykjanes Peninsula. The authors found ordinary kriging algorithm given by [17] to be simple and appropriate. Kriging algorithms use geostatistical

measurements to find an optimal set of weights used for the interpolation, calculated from a semivariogram (inverse related to the covariance) estimated from the data. The ordinary kriging algorithm requires the motion field to be both first and second order stationary [18], and the estimated semivarograms of each of the three GPS components to be fitted with a Gaussian semivariogram model [17]. The Gaussian semivariogram model includes a preconception about the shape of the semivariogram (how the amplitude of the semivariogram increases with distance). Based on the observation of the GPS vectors, the authors argue that the motions at the Reykjanes Peninsula are east-west oriented and anisotropic. Furthermore, the vertical motions are partly localized, e.g., with some local subsidence at Svartsengi [19]. Hence the motion field is in general not stationary, and thus the averaged semivariograms do not produce the appropriate shape that is needed for the Gaussian semi- variogram model. However the authors highlight that the averaged semivariograms strongly indicate that the motion field is approximately first and second order stationary within a distance of at least 200 pixels (18 km) from any arbitrary chosen location (point) at the Reykjanes Peninsula area. Hence an appropriate shape for the Gaussian semivariogram modeling can be achieved by only using semivariogram data within a distance of 200 pixels. The spatial consistency of the GPS data is preserved in the kriged motion maps. Furthermore, both the east-west tendency of the horizontal motions and the localized subsidence pattern at Svartsengi appears to be preserved. Accurate interpolation of the subsidence pattern at Svartsengi is also supported by previous studies of the motion field at the area [19]. The authors report an example of consistency between the interpolated GPS data and InSAR data . The good agreement of the two independent complementary data sets indicates a successful interpolation of the sparse GPS data. The ordinary kriging algorithm may not always be applicable. This was the case in the study of ice flow by [20], where motions were highly anisotropic and localized. In their

case, both time series of digital elevation maps (DEMs) of the ice surface and aerial photographs were available. Thus they found it appropriate to use cubic spline fits of available sparse ground observations, together with knowledge of the surface patterns from the aerial photographs and by assuming smoothly varying horizontal ice flow parallel to flow lines with the aid of the DEMs. Another type of localized and anisotropic surface movements are discontinuities because of seismic or aseismic deformation. Often, there exists a physical model that describes the general patterns of such motions. One possibility is to remove the model from the GPS observations, interpolate the residuals (e.g., with the ordinary kriging algorithm) and add back in the model. Such residuals are expected to be approximately a stationary random field, which is the most appropriate form for kriging algorithms.

Energy Functions

The authors propose the following general form of a total energy function used to optimize the two motion maps x_1 and x_2 in equation (6):

$$U(x_1, x_2 \mid y) = U_1(x_1, x_2) + U_2(y \mid x_1, x_2) =$$
$$= U_{11}(x_1) + U_{22}(x_2) + U_2(y \mid x_1, x_2) \qquad (10)$$

where the former step is an extension of the energy functions in equation (9), and the later step is achieved by assuming independence between the likelihoods of x_1 and x_2. $U_{11}(x_1)$ and $U_{22}(x_2)$ are then related to the neighbourhood structure of x_1 and x_2, respectively, and $U_2(y \mid x_1, x_2)$ expresses the relationship of the two-dimensional motion field to the unwrapped InSAR image *y* as given in equation (6). Then the author propose the following energy function to optimize equation (6):

$$U_2(y \mid x_1, x_2) = \gamma \sum_n \left(y_n + [x_{1n}, x_{2n}][u_1, u_2]^T \right)^2 \tag{11}$$

where *n* is a pixel number and γ_2 is a constant.

The authors invoke the smoothness of the first derivatives of x_1 and x_2, implemented as a penalization on the second derivative [12], with the approximations

$$U_{11}(x_1) = \gamma_{11} \sum_i \sum_j \left(x_{1i-1,j} + x_{1i+1,j} - 4x_{1i,j} + x_{1i,j-1} + x_{1i,j+1} \right)^2 \tag{12}$$

$$U_{22}(x_2) = \gamma_{22} \sum_i \sum_j \left(x_{2i-1,j} + x_{2i+1,j} - 4x_{2i,j} + x_{2i,j-1} + x_{2i,j+1} \right)^2 \tag{13}$$

where *i,j* are the row and column numbers, respectively, and γ_{11} and γ_{22} are constants. By using equation (12) and (13), the authors have assumed the motion field to be smoothly varying. The smoothness requirements were the only prior expectations about the random field used in their work. It serves the important purpose of preserving the correlated relationship of the image pixel values. The U_1 term in equation (10) may consist of various types of prior expectations. As an example, in study of ice flow [20], authors used an assumption of having horizontal ice flow parallel to the flow lines at the surface, implemented with aid of digital elevation map.

The energy function in equation (10) utilizes the relationship of the motion field images to the known image *y*. Sparse values of the motion field images x_1 and x_2 are known from the GPS

observations and are used to initialize the process. The interpolated initial motion maps (the GPS observations) can also be utilized into the MRF models by extending equation (10) as

$$U(x_1, x_2 \,|y, x_{i1,} x_{i2,}) = U_1(x_1, x_2) + U_3(y, x_{i1}, x_{i2} \,|x_{1,} x_{2,}) =$$

$$= U_{11}(x_1) + U_{22}(x_2) + U_2(y \mid x_1, x_2) + U_{I1}(x_{I1} \mid x_1) + + U_{I2}(x_{I2} \mid x_2) \quad (14)$$

where x_{I1} *and* x_{I2} are the estimated initial values of x_1 and x_2 respectively. As in equation (10), independence is assumed between the likelihoods of x_1 and x_2 , which leads to the final step in equation (14).

The expected spatially variable accuracy of the interpolation (kriging) results can be incorporated in the regularization by introducing an ‘‘uncertainty image’’ w. Authors use a method introduced by [17] to create the uncertainty image along with the kriging of the sparse motion field measurements. In his method, the kriging results are expected to be most accurate at, and close to, pixels corresponding to the GPS locations but become more uncertain with distance from them. No uncertainty is assigned to pixels with GPS observations and the certainty then decreases away from them. In the uncertainty image, a value of one means no uncertainty and a value of zero means no certainty. The spatial accuracy of the interpolation may also depend on variable uncertainty assigned to each GPS vector. It is possible to incorporate those variable errors in the uncertainty image, by assigning suitable uncertainty value to pixels with GPS observations. The initial values and the uncertainty image are utilized into the MRF regularization by penalizing the motion maps for deviating from the initial results. The penalization is then weighted with the uncertainty image. This is done by using the energy terms

$$U_{11}(x_{I1} \mid x_1) = \gamma_{I1} \sum_n \left(w_{1n} \left(x_{i1_n} - x_{1n} \right)^2 \right) \tag{15}$$

$$U_{12}(x_{I2} \mid x_2) = \gamma_{I2} \sum_n \left(w_{2n} \left(x_{i2_n} - x_{2n} \right)^2 \right) \tag{16}$$

for the motion field image x_1 and x_2, respectively, where *n* is pixel number, x_{I1_n} and x_{I2_n} are the initial values at the pixel *n*, w_{1n} and w_{2n} are the estimated uncertainty of the initial values at the pixel *n* and γ_{I1} and γ_{I2} are constants. Because of the uncertainty images, the penalization in equations (15) and (16) becomes strongest at and close to pixels with GPS values and decreases with distance from them. The energy function in equation (14) has the advantage of utilizing both the relationship of the motion maps to InSAR and GPS observations.

Simulated Annealing Optimization

The simulated annealing algorithm proposed by S. Gudmundsson and F. Sigmundsson for the optimization of the two realization images x_1 and x_2 is the following:

1. Choose initial images x_1 and x_2, (e.g., by kriging) and set the initial temperature $T = T_0$.
2. $k = 2$, where k is a pixel number.
3. Increase or decrease x_{1k} with equal probability by a value of Δx, which gives a new image $x_1^{'}$.

4. Calculate $r_{1k} = \left[p_T(x_1^{'}) / p_T(x_1)\right] = \exp\left\{-\left[U(x_1^{'}) - U(x_1)\right]/T\right\}$.

5. If $r_{1k} > \mu[0,1]$, *then* $x_{1tk} = x_{1k}^{'}$; *otherwise* $x_{1tk} = x_{1k}$.

6. $k = k+1$, *if* $k \le M$, go to step 3; otherwise, go to the next step (M is the total number of pixels).

7. $x_1 = x_{1t}$.

8. $k = 1$.

9. Increase or decrease x_{2k} with equal probability by a value of Δx, which gives a new image $x_2^{'}$.

10. Calculate $r_{2k} = \left[p_T(x_2^{'}) / p_T(x_2)\right] = \exp\left\{-\left[U(x_2^{'}) - U(x_2)\right]/T\right\}$

11. $r_{2k} > \mu[0,1]$, *then* $x_{2tk} = x_{2k}^{'}$; *otherwise* $x_{2tk} = x_{2k}$

12. $k = k+1$, *if* $k \le M$, go to step 9; otherwise, go to the next step next step.

13. $x_2 = x_{2t}$.

14. $T = T \times cool$, where cool <1 is a constant.

15. Go to step 2.

The authors separated the optimization into two steps. First x_1 is updated for given x_2, and then x_2 for a given x_1. Then these steps are repeated until a satisfactory result is achieved. The energy function U is given by either equation (10) or (14). The algorithm uses a nonrecursive update of the pixel values . The MRF model favors low energy states by associating them with high probabilities. The Markov property of the random field is utilized when calculating the ratio of the image probability states with and without updated pixel value (steps 4 and 10 in algorithm 1). As the author emphasizes all terms in the probability formulation not directly related to the pixel under consideration disappear due to the Markov

property. This is evident when implementing the associated energy functions into the calculation of the image probability ratio in steps 4 and 10, i.e., all terms in the summation in equations (11), (12), (13), (15), and (16) not directly related to the updated pixel value cancel out in the probability ratio. Furthermore, the energy terms in equations (13) and (16) (energy terms not related to x_1) cancel out in step 4 and in equations (12) and (15) (energy terms not related to x_2) in step 10. In the algorithm, $\mu[0,1]$ is a random number ranging from 0 to 1, selected from a uniform random generator. This simulated annealing algorithm chooses a new energy stage if the probability ratio is larger than random number within the [0,1] interval. This allows the algorithm to explore various combinations of the motion maps, and hence avoid local minima. As $T \to 0$, the effects from the random generator vanish. The constant cool in algorithm 1 establishes the temperature fall. After full annealing, the algorithm selects the motion maps with the highest probability.

Parameters

As highlighted by the authors the ratio of the γ coefficients represents combination of both scaling and weighting of each of the energy terms in the optimization. Indeed the energy functions represent different types of quantities. Furthermore, evaluation of suitable values for these parameters is not a simple task. By using various experiments, the authors found $\gamma_2 = 10$ in equation (11), $\gamma_{11} = 1$ and $\gamma_{22} = 1$ in equations (12) and (13), respectively, and $\gamma_{11} = \gamma_{12} = 10$ in equations (15) and (16), to work well for their data. Relationship of the motion maps to the InSAR observations is reflected in equation (11), i.e., projection of the motion maps on a unit vector is known at all pixels. Thus, the energy term in equation (11) is given a relatively strong weight in the optimization. An infinite set of solutions exists for

equation (11). Hence, the authors use as an additional constraint (a prior expectation about the motion field) an assumption of having a smoothly spatial varying motion field (equations (12) and (13)). Those smoothness requirements also reduce the effects of high frequency noise errors in the InSAR data. A smoothly varying motion field is not always the case, e.g., when there are discontinuities due to seismic deformation. Strong smoothness requirements can result in oversmoothing of narrow deformation features. Here they keep the weights of equations (12) and (13) small but under the consideration of achieving acceptable spatial correlation in the output motion maps. The energy terms in equations (15) and (16) express the relationship of the output motion maps to the sparse GPS data. Those energy terms also tend to smooth the output data. The smoothing effects are though small compared to those of equations (12) and (13). Here we keep the constraint in equations (15) and (16) much weaker than in equation (11). [25] The weights may depend on the nature of the data. In [20] authors found the same values of γ_2, γ_{11}, and γ_{22} to be suitable to optimize 3-D motion maps at the 1996 Gjalp eruption site in Vatnajoull, Iceland. Opposite to the author GPS data, their sparse ground observations of the vertical, east, and north components of the motion field were not all conducted at the same locations. Because of this, it was better to use only half the values we use for γ_{I1} and γ_{I2} in that case. The author use $T_0 = 0$, $\Delta x = 0.1$, and $cool = 0.99$ in algorithm 1, and the process is terminated for $T < 0.1$.

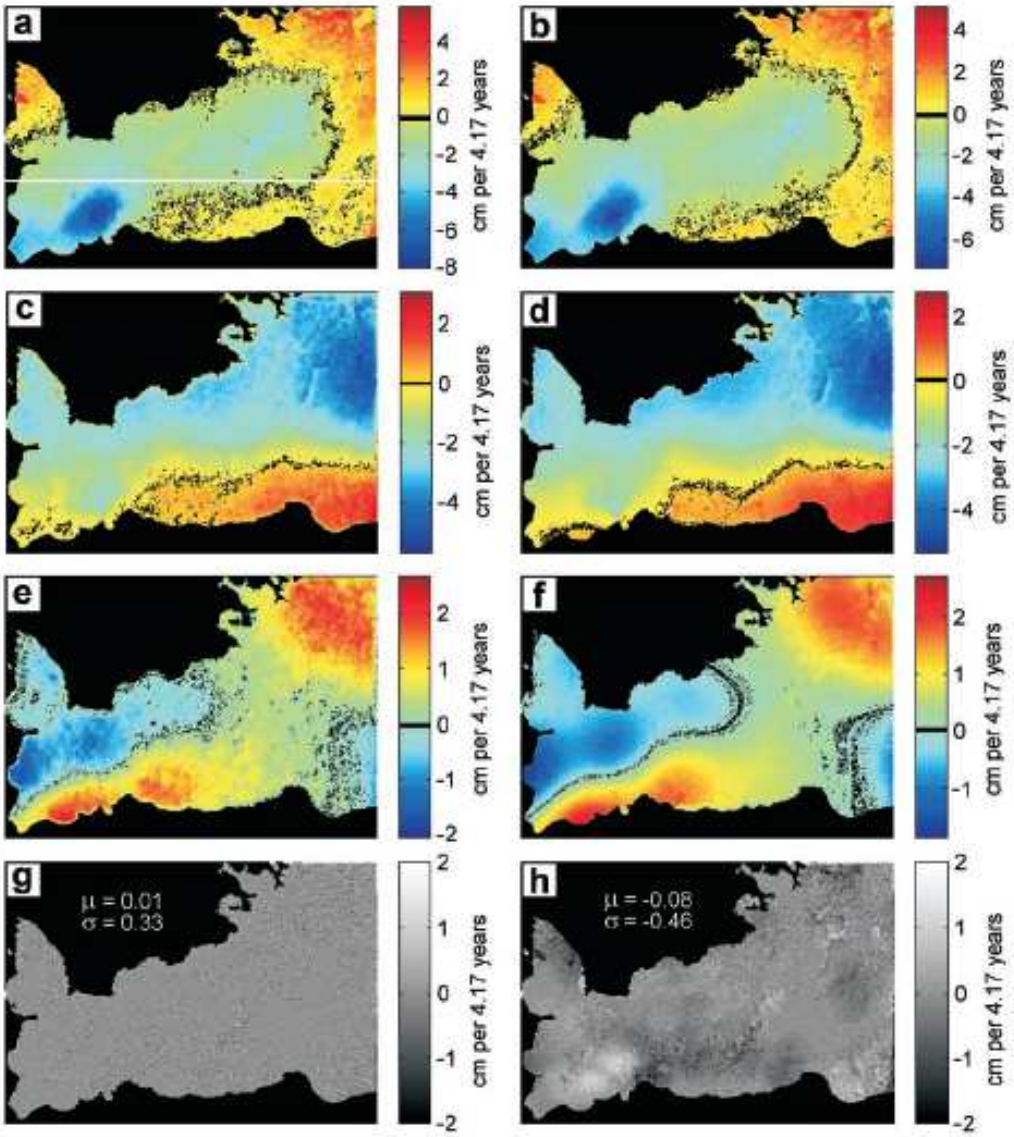

Figure 1. S. Gudmundsson and F. Sigmundsson results (from [8])

In figure 1 ground movements at the Reykjanes Peninsula inferred by using the GPS measurements and 4.17 years interferogram are shown. The results are show of using only the relationship to the InSAR observation in equation (10), and the relationship to both the InSAR and GPS observations in equation (14), in the MRF regularization. (a), (c), (e) The vertical, east, and north motion maps, respectively, inferred by optimizing equation (10). (b), (d), (f)

The same from optimizing equation (14). (g) Residual error between the 4.17 years interferogram and projection of the images in Figures 1a, 1c, and 1e into the slant range of the SAR satellite, and the mean value (m) and standard deviation (s) of the residuals. (h) The same for the images in Figures 1b, 1d, and 1f.

The Samsonov and Tiampo method

The method proposed by Samsonov and Tiampo is based on a random field theory and Gibbs–Markov random fields equivalency within Bayesian statistical framework. It is slightly different from the method proposed by S. Gudmundsson and F. Sigmundsson. This method minimizes the energy function without the smoothness criteria, and thus without the smoothness term thus allowing an analytical optimization of the Gibbs function.

Theoretical background

Samsonov and Tiampo start their paper giving an introduction to the Bayesian inference. Bayesian inference is a theory of fundamental importance in estimation and decision-making. It is based on the Bayes theorem, which relates posterior and prior probabilities according to the following equation:

$$P(x \mid y) = \frac{P(x)P(y \mid x)}{P(y)} \propto P(x)P(y \mid x) \tag{17}$$

where $P(x \mid y)$ is the posterior distribution, $P(x)$ is the prior distribution, $P(y \mid x)$ is the conditional probability or the likelihood of the observation *d*, and $P(y)$ is the density of d which is constant when *d* is given and therefore can be skipped in the future derivations.

The authors highlight that in Bayes estimation, a risk is minimized to obtain the optimal estimate. The Bayes risk of estimate x^* is defined as

$$R(x^*) = \int_{x \in X} C(x^*, x) P(x \mid y) dx \tag{18}$$

where $C(x^*, x)$ is a cost function defined as

$$C(x^*, x) = \begin{cases} 0, \ if \ \ \|x^* - x\| \le \delta \\ 1, \ otherwise \end{cases} \tag{19}$$

where δ is any small constant.

The Bayes risk can be calculated by substitution of (19) in (18)

$$R(x^*) = \int_{x:\|x^* - x\| > \delta} P(x \mid y) dx = 1 - \int_{x:\|x^* - x\| \le \delta} P(x \mid y) dx \tag{20}$$

As $\delta \to 0$ the above equation can be approximated by the following:

$$R(x^*) = 1 - kP(x \mid d) \tag{21}$$

where *k* is the volume of the space containing all points for which $\|x^* - x\| \le \delta$. Therefore, the minimization of (21) is equivalent to maximization of $P(x \mid y)$.

The poster distribution $P(x \mid y)$ can be calculated from the prior distribution and likelihoods in a way given by Bayes theorem (17). The prior distribution can be presented according to the Hammersley-Clifford theorem in a form

$$P(x) = \frac{1}{Z} e^{-U(x)/T} \tag{22}$$

where U is the energy function of corresponding Gibbs random field and

$$Z = \sum_{x \in X} e^{-U(x)/T} \tag{23}$$

is a normalization constant called *partitioning function* and T is a *temperature* which is assumed to be equal to one and skipped in later derivations. Then likelihoods can be calculated in a similar way by

$$P(y \mid x) = \frac{1}{\prod_{i=1}^{N} \sqrt{2\pi\sigma_i^2}} e^{-U(y|x)} \tag{24}$$

where the energy function is

$$U(y \mid x) = \sum_{i=1}^{N} \frac{(x_i - y_i)^2}{2\sigma_i^2} \tag{25}$$

The authors rewrite the total energy function in the following form:

$$U(x \mid y) = U(y \mid x) + U(x) = \sum_{i=1}^{N} \frac{(f_i - d_i)^2}{2\sigma_i^2} + U(f) \tag{26}$$

GPS and DInSAR analytical integration

The author's goal is to calculate three components of the velocity vector at each grid point from three known datasets: ascending and descending DInSAR interferograms and GPS velocities at the sparse locations. In order to solve this problem is needed to opportunely define the correct Gibbs energy. The prior distribution of (26) is the initial assumption about the authors' model, which in general may be correct or incorrect. As focused by Samsonov and Tiampo, if the assumption is incorrect and thus carries some misleading information then the posterior distribution will be misleading also, at least in part. Therefore, since the accuracy of initial assumptions is unknown here, Samsonow and Tiampo propose not to use it and draw all information from the data only.

Two DInSAR interferograms can be related to components of the velocity vector according to the following equation:

$$V_{LOS}^{2i} = \left[v_x^i; v_y^i, v^i{}_z\right]\left[S_x^2, S_y^2; S_z^2\right]^T$$
$$V_{LOS}^{1i} = \left[v_x^i; v_y^i, v^i{}_z\right]\left[S_x^1, S_y^1; S_z^1\right]^T \qquad (27)$$

where V_{LOS}^{1i} and V_{LOS}^{2i} are the known interferograms defined on a grid of *N* points, $\left[v_x^i; v_y^i, v^i{}_z\right]$ are unknown components of the velocity vector and $\left[S_x^1, S_y^1; S_z^1\right]$ and $\left[S_x^2, S_y^2; S_z^2\right]$ are unit vectors pointing from the ground toward the satellite.

The GPS velocities are known only at a few locations

$$V^i = \left[v_x^i; v_y^i, v^i{}_z\right] \qquad (28)$$

Some interpolations technique such as kriging is required by the authors in order to fill in GPS velocities at the DInSAR grid points. Kriging is a method of interpolation which predicts unknown values from data observed at known locations. This method uses a variogram to express the spatial variation, and it minimizes the error of predicted values, which are estimated by spatial distribution of the predicted values [21], [22].

Samsonov and Tiampo rewrite the Gibbs energy function in the following form, where the first two terms correspond to DInSAR and the last three terms correspond to GPS:

$$u\left(v_x,v_y;v_z\right)=\sum_{i=1}^{N} C_{ins}^{1i}\left(V_{LOS}^{1i}-S_x^1 v_x^i-S_y^1 v_y^i-S_z^1 v_z^i\right)^2+C_{ins}^{2i}\left(V_{LOS}^{2i}-S_x^2 v_x^i-S_y^1 v_y^i-S_z^1 v_z^i\right)^2+$$

$$C_x^i\left(V_x^i-v_x^i\right)^2+C_y^i\left(V_y^i-v_y^i\right)^2+C_x^i\left(V_z^i-v_z^i\right)^2 \qquad (29)$$

with coefficients

$$C_{ins}^{1i}=\frac{1}{2\left(\sigma_{ins}^{1i}\right)^2} \quad C_{ins}^{2i}=\frac{1}{2\left(\sigma_{ins}^{2i}\right)^2} \quad C_x^i=\frac{1}{2\left(\sigma_{ix}^i\right)^2} \quad C_y^i=\frac{1}{2\left(\sigma_y^i\right)^2} \quad C_z^i=\frac{1}{2\left(\sigma_z^i\right)^2} \qquad (30)$$

where σ's are standard deviations of the measurements.

Equation (13) is a function of variables $3\times N$ variable $\left[v_x^i,v_y^i,v_z^i\right]$ where N is the number of grid points. It consists of N nonnegative terms corresponding to the same index i. Therefore, the function $u\left(v_x,v_y,v_z\right)$ reaches its global minimum when each subgroup with the same index i is minimal, and the first partial derivatives $\partial u/\partial v_x^i$, $\partial u/\partial v_y^i$, $\partial u/\partial v_z^i$, are equal to zero.

$$\frac{\partial u}{\partial v_x^i} = -2C_{ins}^{1i}S_x^{1i}\left(V_{LOS}^i - S_x^{1i}v_x^i - S_y^{1i}v_y^i - S_z^{1i}v_z^i\right) - 2C_{ins}^{2i}S_x^{2i}\left(V_{LOS}^i - S_x^{2i}v_x^i - S_y^{2i}v_y^i - S_z^{2i}v_z^i\right)$$

$$- 2C_x^i\left(V_x^i - v_x^i\right)$$

$$\frac{\partial u}{\partial v_y^i} = -2C_{ins}^{1i}S_y^{1i}\left(V_{LOS}^i - S_x^{1i}v_x^i - S_y^{1i}v_y^i - S_z^{1i}v_z^i\right) - 2C_{ins}^{2i}S_y^{2i}\left(V_{LOS}^i - S_x^{2i}v_x^i - S_y^{2i}v_y^i - S_z^{2i}v_z^i\right)$$

$$- 2C_y^i\left(V_y^i - v_y^i\right)$$

$$\frac{\partial u}{\partial v_z^i} = -2C_{ins}^{1i}S_z^{1i}\left(V_{LOS}^i - S_x^{1i}v_x^i - S_y^{1i}v_y^i - S_z^{1i}v_z^i\right) - 2C_{ins}^{2i}S_z^{2i}\left(V_{LOS}^i - S_x^{2i}v_x^i - S_y^{2i}v_y^i - S_z^{2i}v_z^i\right)$$

$$- 2C_z^i\left(V_z^i - v_z^i\right) \qquad (31)$$

This set of three linear equations with three unknowns can be constructed for each grid point. The author emphasize that it is always solvable when the determinant of the matrix of coefficients is not zero. It can be shown that this condition is always true when the coefficients (30) are not zeros. Because this is the case in every instance, the exact analytical solution can be easily calculated.

The solution of the set of (31) is the standard inverse problem of the form $X = A^{-1}\bar{u}$. Matrix *A* in this equation is nonsingular and the inverse matrix A^{-1} is continuous on any point where $C_x, C_{y,} C_z$ are not null at the same time, which occurs in almost all cases. Therefore, a unique, stable solution always exists. However, in numerical calculations, the fact that $\det A$ can become very small when errors are big gives instabilities of the type 0/0 and the limit, which always exists, must be calculated carefully.

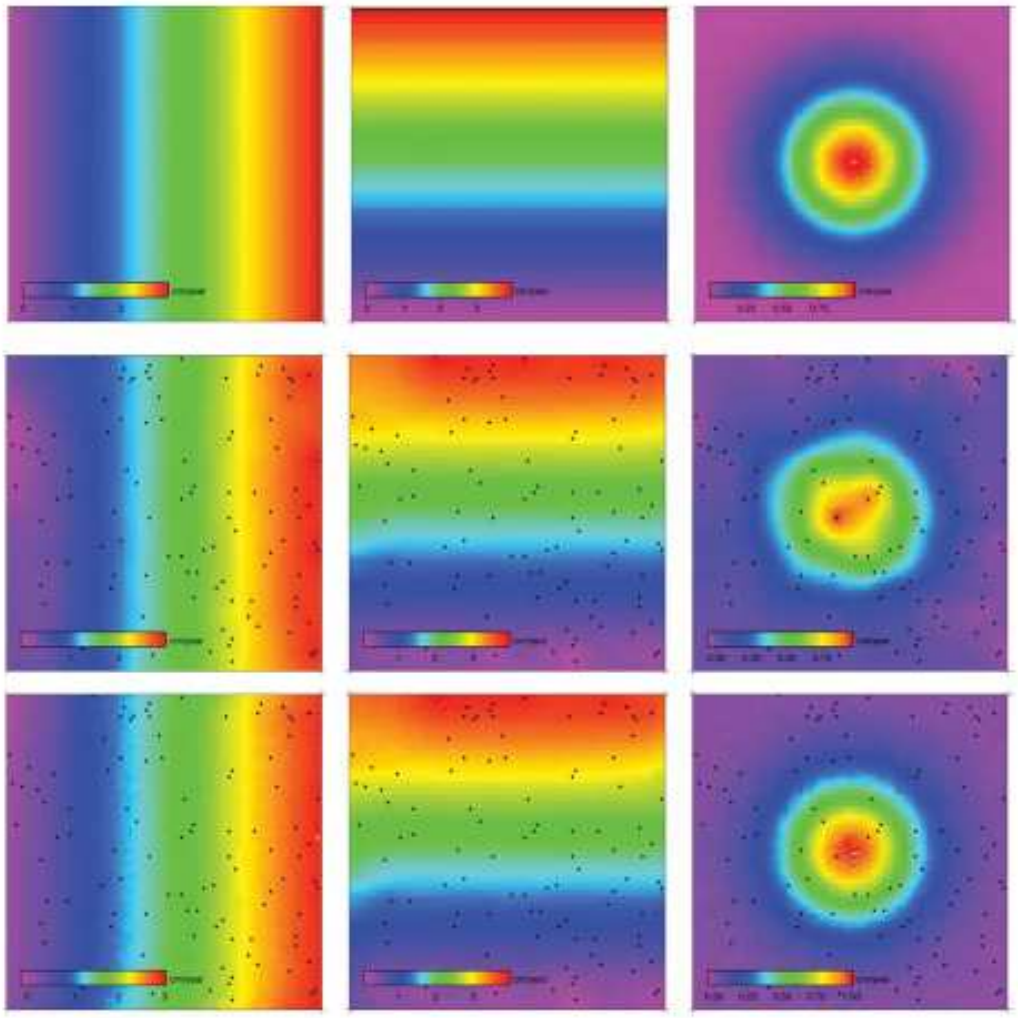

Figure 2. Samsonov and Tiampo results from [9]

In figure 2 results relevant to a synthetic case study performed by Samsonov and Tiampo is shown. In the first row original modeled components of surface velocity field that are to be restored are reported. In the second row the components of the velocity field interpolated from sparse GPS locations by ordinary kriging is shown. In the third row the restored components of the velocity field after applying GPS-DInSAR optimization are reported.

Chapter 2

The SISTEM method

Introduction

In this chapter the mathematical formulation of the SISTEM method is reported. The proposed methodology was tested on both synthetic and experimental data. In particular the latter from GPS and DInSAR measurements carried out on Mt. Etna during the 2003-2004 time interval. In order to appreciate the results accuracy standard estimated errors are provided. These tests also allow optimising the choice of specific parameters of this algorithm.

Both methodology and results reported in this chapter have been submitted to IEEE Geoscience and Remote Sensing [23] and are under review.

Mathematical Background

In this section we set out a few well known points, from continuum mechanics and geodesy, which are fundamental to implement the method for integrating GPS and DInSAR data introduced in this paper.

Let us assume that a geodynamic process (e.g. intrusions of magma or earthquakes) deforms a portion of Earth's surface; under the hypothesis of infinitesimal and homogeneous strain we define an arbitrary point P, having position $x_0=(x_{10}, x_{20}, x_{30})$, and N surrounding experimental points (EPs) whose positions and displacements are respectively $\boldsymbol{x}_{(n)}=(x_{1(n)}, x_{2(n)}, x_{3(n)})$ and $\boldsymbol{u}_{(n)}=(u_{1(n)}, u_{2(n)}, u_{3(n)})$ where $n=1..N$. Under such a hypothesis, adopting a linear approach, the

problem of estimating the displacement components U_i (i=1..3) of the point *P*, from the experimental data $\boldsymbol{u}_{(n)}=(u_{1(n)}, u_{2(n)}, u_{3(n)})$, can be modelled by the *N* equations [24]:

$$u_{i(n)}(x) = H_{ij}\Delta x_{j(n)} + U_i \ \ (i, j = 1..3) \tag{1}$$

where $\Delta x_{j(n)}=x_{j(n)}-x_{j0}$ are the components of the vector distance between the n^{th} EP experimental points and the arbitrary point P, while $H_{ij}=\dfrac{\partial u_i}{\partial x_j}$ are the elements of the displacement gradient tensor. In equation (1) the matrix **H** can be broken down into a symmetric and an anti-symmetric part as **H=E+Ω**. The symmetric part **E** is the well known strain tensor defined as:

$$E = \varepsilon_{ij} = \frac{1}{2}(H_{ij} + H_{ji})\underline{e_i} \otimes \underline{e_j} = \begin{bmatrix} \varepsilon_{11} & \varepsilon_{12} & \varepsilon_{13} \\ \varepsilon_{12} & \varepsilon_{22} & \varepsilon_{23} \\ \varepsilon_{13} & \varepsilon_{23} & \varepsilon_{33} \end{bmatrix} \tag{2}$$

and the antisymmetric part **Ω** is the rigid body rotation tensor defined as**:**

$$\Omega = \omega_{ij} = \frac{1}{2}(H_{ij} - H_{ji})\underline{e_i} \otimes \underline{e_j} = \begin{bmatrix} 0 & -\omega_3 & \omega_2 \\ \omega_3 & 0 & -\omega_1 \\ -\omega_2 & \omega_1 & 0 \end{bmatrix} \tag{3}$$

Here e_i is the canonical base vector of the Cartesian reference system and $\otimes$ is the tensor product.

It is straightforward to show that the *3N* equations of type (1) give a linear matrix equation of the following form:

$$Al = u \tag{4}$$

where **A** is the *3N*12* design or coefficient matrix [25], **l=[** $U_1\ U_2\ U_3\ \varepsilon_{11}\ \varepsilon_{12}\ \varepsilon_{13}\ \varepsilon_{22}\ \varepsilon_{23}\ \varepsilon_{33}\ \omega_1\ \omega_2\ \omega_3]^T$ is the column vector of unknown parameters and $\mathbf{u}=[\mathbf{u}_{(1)}\ \mathbf{u}_{(2)}\ \ldots\ \mathbf{u}_{(n)}]^T$ is the column observation vector, usually referring to displacement vectors measured at *N* geodetic benchmarks.

Assuming a uniform strain field and re-writing the previous linear equation (4) as *Al=u+e*, where *e* is the residual vector that models the stochastic nature of the estimation problem**,** a suitable method to solve the system is the Weighted Least Squares (WLS) which gives the expression (5) as a suitable formula to estimate the unknown vector *l*

$$\hat{l} = (A^T W A)^{-1} A^T W u \tag{5}$$

where **W** is the inverse of the data covariance matrix **C**.

According to the modified least squares (MLS) approach proposed by [25], based on the adjustment of the covariance matrix , we use the matrix **C'** which is a weighted version of the matrix **C**. Following the suggestion given by [25, 26], the weighting is given as:

$$C' = C \exp(-\frac{d_{(n)}}{d_0}) \tag{6}$$

where $d_{(n)}$ is the distance between the n^{th} EP and the arbitrary point P, and d_0 is a distance-decaying constant defining the "level of locality" of the estimation; hereafter, the parameter d_0 is defined as "locality".

Likewise most previous methods [27, 28, 29] the [25] approach is used to interpolate the strain among benchmarks of geodetic networks where ground deformations are measured by comparing geodetic surveys.

The Simultaneous and Integrated Strain Tensor Estimation from geodetic and satellite deformation Measurements (SISTEM) approach

In this section we describe the SISTEM method for estimating the gradient displacements tensor taking into account both the *in situ* geodetic measurements and the satellite deformation measurements. In particular, we implement this method for the simultaneous integration of the 3D components of displacements measured by a GPS network and the DInSAR LOS displacement map, but it can be easily extended to other kind of terrestrial geodetic measurements.

A DInSAR interferogram can be related to the components of the displacement vector of an arbitrary point *P* according to the following equation:

$$D_{LOS}^{P} = [U_1, U_2, U_3][S_x^P, S_y^P, S_z^P]^T \quad (7)$$

where D_{LOS}^{P} is the LOS displacements, at the point P on the Earth's surface, U_1, U_2 and U_3 are the unknown displacements vector components, and $[S_x^P S_y^P S_z^P]$ is a unit vector pointing from the point *P* toward the satellite. In order to create a highly accurate surface motion map, with the same spatial resolution of DInSAR image, we have included the DInSAR data into the global strain estimation methods previously introduced. It is straightforward to demonstrate that for integrating GPS and DInSAR data, these last in the form defined by (7), the

estimation problem can be expressed in the usual form $Al=u+e$ where the coefficient matrix A assumes the following structure:

$$A=\begin{bmatrix}
1 & 0 & 0 & \Delta x_{1(1)} & \Delta x_{2(1)} & \Delta x_{3(1)} & 0 & 0 & 0 & 0 & \Delta x_{3(1)} & -\Delta x_{2(1)} \\
0 & 1 & 0 & 0 & \Delta x_{1(1)} & 0 & \Delta x_{2(1)} & \Delta x_{3(1)} & 0 & -\Delta x_{3(1)} & 0 & \Delta x_{1(1)} \\
0 & 0 & 1 & 0 & 0 & \Delta x_{1(1)} & 0 & \Delta x_{2(1)} & \Delta x_{3(1)} & \Delta x_{2(1)} & -\Delta x_{1(1)} & 0 \\
. & . & . & . & . & . & . & . & . & . & . & . \\
. & . & . & . & . & . & . & . & . & . & . & . \\
. & . & . & . & . & . & . & . & . & . & . & . \\
1 & 0 & 0 & \Delta x_{1(N)} & \Delta x_{2(N)} & \Delta x_{3(N)} & 0 & 0 & 0 & 0 & \Delta x_{3(N)} & -\Delta x_{2(N)} \\
0 & 1 & 0 & 0 & \Delta x_{1(N)} & 0 & \Delta x_{2(N)} & \Delta x_{3(N)} & 0 & -\Delta x_{3(N)} & 0 & \Delta x_{1(N)} \\
0 & 0 & 1 & 0 & 0 & \Delta x_{1(N)} & 0 & \Delta x_{2(N)} & \Delta x_{3(N)} & \Delta x_{2(N)} & -\Delta x_{1(N)} & 0 \\
S_x^P & S_y^P & S_z^P & 0 & 0 & 0 & 0 & 0 & 0 & 0 & 0 & 0
\end{bmatrix} \quad (8)$$

While the measured data vector assumes the form:

$$u=[u_{1(1)}u_{2(1)}u_{3(1)}...u_{1(n)}u_{2(n)}u_{3(n)}D_{LOS}^P]^{\mathrm{T}} \quad (9)$$

It should be observed that the A matrix consists of *3N+1* rows: the first *3N* rows can be viewed as *N* blocks of three equations which represent information on the GPS position of each single EP with respect to the arbitrary point P, while the last equation refers to the corresponding DInSAR data. The interested reader can verify that expressions (8) and (9) have been resembled from those given by [25], which refers to the GPS measure only.

We emphasize that the SISTEM method is a point-wise oriented approach. This means that, at the unknown point *P*, SISTEM solves the WLS problem by taking into account the surrounding GPS points and only the DInSAR data coincident with the point *P*. Therefore the spatial correlation of DInSAR data is not taken into account. Finally, the point-wise approach

implies that for areas where DInSAR data is missed (e.g. low coherency, decorrelated areas, etc.) the SISTEM does not provide the integrated deformations.

In order to solve the problem by using the WLS method it is necessary to modify the covariance matrix structure of observation by adding the variance of DInSAR data points. For this purpose we estimated the variance of the DInSAR data directly from the interferogram by using a sample semi-variogram $\gamma(h_c)$ (eq. 10) [30, 31]

$$\gamma(h_c) = \frac{1}{2N}\sum_{i=1}^{N}\left[d(r_i) - d(s_i)\right]^2 \tag{10}$$

where h_c is a classified separation distance.

The weight function (7) has been used only on GPS data, because for each arbitrary point P the D_{LOS}^{P} measurement is known.

In this method, the only parameter that needs to be appropriately chosen is the parameter d_0 in order to define the level of locality of the estimation. As suggested by [26] we have related d_0 with the mean inter-distance between neighbour stations. In particular let N be the number of EPs point of the network and K_i be the set of M nearest stations in the circle centered at the i station. It is obvious that the radius of this circle depends on i. We propose the following empirical formula to evaluate d_0:

$$d_0 = \frac{1}{NM}\sum_{i=1}^{N}\sum_{j\in K_i} d_{ij} \tag{11}$$

The optimal value of *M* depends on the topology of the network; based on several trials, we have empirically found that for random configurations M ranges between 4 and 6.

It should be noted that the effects of the locality d_0 are the following: only the points closer than about d_0 to P give a significant contribution to its estimation; the uniform distribution of the strain is required only in a neighbourhood of each computation point; for points P far away the EPs the DInSAR data becomes the dominant information source.

In order to estimate the goodness of the SISTEM method, we have used the estimated standard error provided by the WLS approach.

A Synthetic case study

The SISTEM method is firstly tested on synthetic interferograms and displacement fields obtained by assuming a specific strain pattern and by using a synthetic topography. As proposed by [9]; the topography is computed according with

$$z(x,y) = z_0 e^{-\left(\left(x^2+y^2\right)/w\right)} \tag{12}$$

where $z(x,y)$ is the elevation at a point {x,y}, z_0 is the initial maximum elevation to the central point, and w is a form factor used to adjust the slope and the size of the hill (Fig.1). In our case z_0 =1000 m and w =1.

The synthetic dataset was generated by assuming a point pressure source [18, 1] (Mogi, 1958; Dzurisin, 2007) defined by:

$$\begin{pmatrix} u_1 \\ u_2 \\ u_3 \end{pmatrix} = \frac{a^3 \Delta P (1-\nu)}{\mu} \begin{pmatrix} \frac{x_1}{R^3} \\ \frac{x_2}{R^3} \\ \frac{d}{R^3} \end{pmatrix} \quad (13)$$

Where u_j *(j=1,3)* are the displacements along the three directions estimated at the point P (x_1, x_2, d), *-d* is the depth of the pressure source and $R = \sqrt{x_1^2 + x_2^2 + d^2}$ is the radial distance of the point P from the centre of the pressure source; ν and μ are the Lame's constants. The pressure source was embedded in an elastic homogeneous Poissonian half-space (Poisson's ratio = 0.25, i.e. λ = μ), and, to take into account the effect of the topography, the simple varying-depth model proposed by [32] was adopted, which consists of assuming a different *-d* at each computation point.

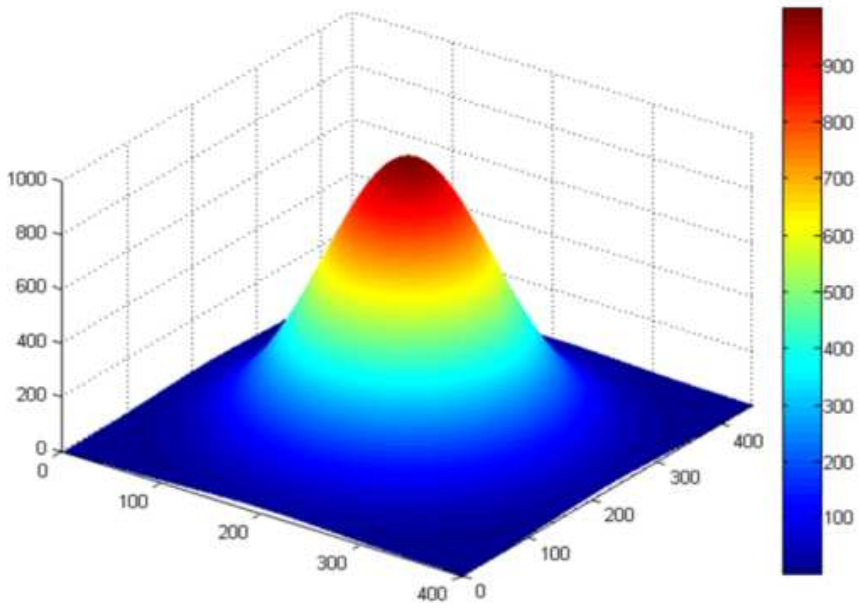

Figure 1. Synthetic topography used for the test

Through the tests the pressure source was centred on a 400x450 grid (cell-size 100 m x 100 m) with μ=30 GPa, depth = 5000 m (with respect to the base of the topography) and with a "strength" parameter ($a^3\Delta P$) = 10^{17} Pa*m^3. The synthetic data set consists of the 3D displacements computed at the EPs and the synthetic interferogram relevant to the considered domain (40 km x 45 km). In the tests we consider the EPs as GPS stations. A Gaussian noise of a form N=(0, σ=5 mm) and N=(0, σ=10 mm) for the horizontal and vertical components respectively were added to the GPS synthetic data. Referring the DInSAR synthetic data, in order to be as realistic as possible we have added a spatial correlated noise with a variance of 3mm calculated on the basis of a fixed covariance matrix by assuming an exponential decay with scale length of 500 meters [33].

In order to estimate the covariance matrix of the synthetic GPS points we have firstly generated a time series representing the pressure value of the Mogi source in the range 0-10^{17} Pa*m^3 at different time instants. This was necessary since the original Mogi model is a static one. According with expression (13) we generated three time series $u_1(t)$, $u_2(t)$ and $u_3(t)$ to evaluate the covariance matrix of the synthetic data set.

Fig. 2 reports the results of the test obtained by using 100 Experimental Points (EP) randomly located assuming a locality (d_0) of 2000 m..

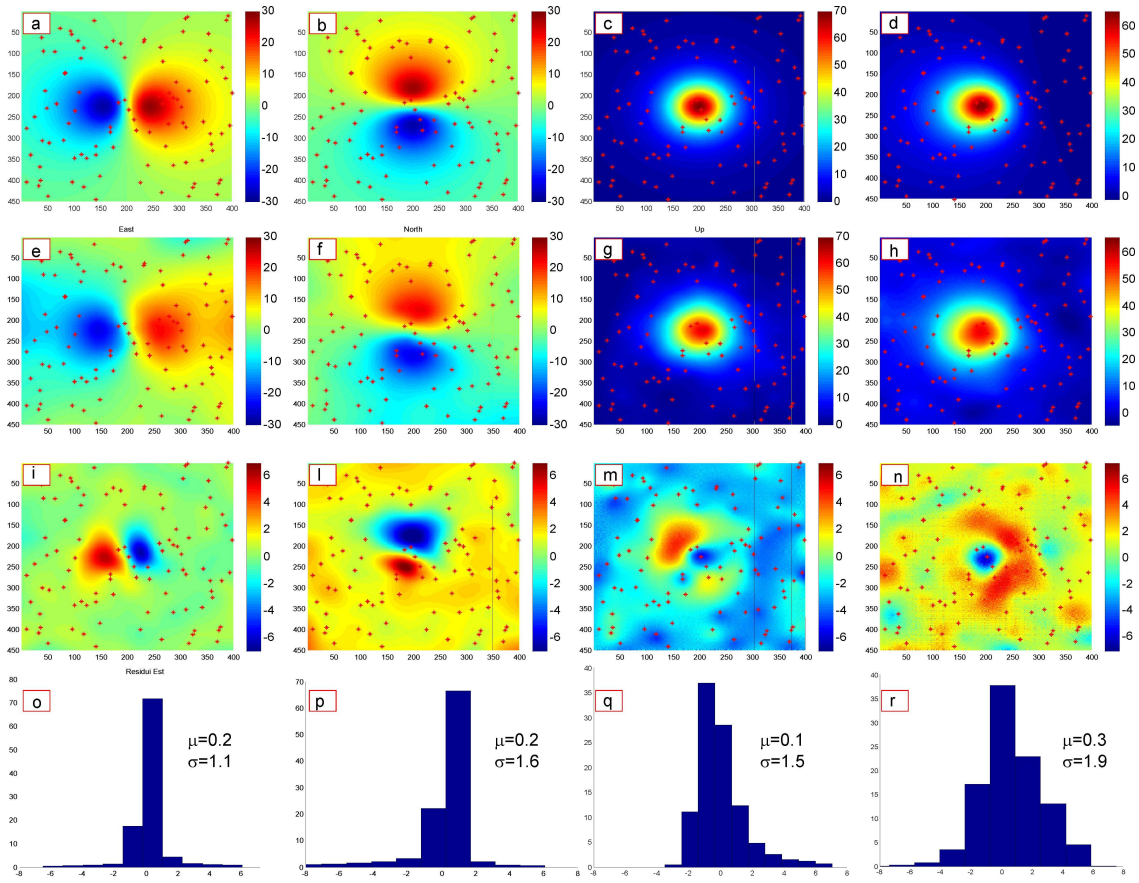

Figure.2 In the frames a,b,c are reported respectively the East, North and Up components of the displacement field while on the frame d is reported the LOS generated on the synthetic topography; the frames a, b, c and d are obtained by using the Mogi source (no error added). The frames e, f, g and h represent the three displacement components and the LOS displacements calculated by SISTEM integration method (for details see the text). In the frames i, l, m and n are reported the residuals of the East, North, Up components and LOS respectively. In the lower row are reported the normalized histograms of the corresponding residual errors, the mean value (μ) and standard deviation (σ).The red point represents the locations of the EPs used for integration. All reported values are in mm.

The original horizontal displacement components have a symmetric shape and range from -30 mm to 30 mm, while the vertical component is very steep at the center area, where it reaches a maximum of about 70 mm.

The components of the displacements calculated by the proposed method are in good agreement with the original data and produce residuals between ±6mm for all the components. The highest residuals are generally localized in areas where both the density of EPs is low and the magnitude of expected deformations is high. The residuals of the vertical component are lower than those relevant to the horizontal ones. The pattern of the residuals of the LOS displacements is peculiar showing a ring-shape feature, around the center area of the image, with the highest residuals on the steepest slopes of the topography. Apart from the scarcity of EPs in these areas, at the origin of this peculiar feature it should be the effect of the difference in considering the distances among points between the models used for computing the synthetic data set [18, 19] and the SISTEM. [32, 34] are, indeed, intrinsically planar, i.e. the distances among points are computed as horizontal, while SISTEM is intrinsically 3D; this difference may produce severe effect on steepest slopes. In order to avoid similar artifacts, in future works we will test the correction proposed by [35], which is more precise than that proposed by [32], but it is more complex and requires more computation time.

The distributions of the errors, reported in the last row of Fig. 2, are slightly biased for all 3D component, but not for the LOS deformations. The reason of such a behavior is due to the random distribution of the EPs. Indeed, by performing a huge number of experiments we found that the best performance is obtained when a regular grid of GPS point is considered. This is rather obvious and has been pointed out by other authors [36]. However, since we think that the random distribution of EPs depicts the actual cases more than a regular distribution, we prefer to maintain these results, even if biased.

Although the integration of DinSAR and GPS data for obtaining the 3D displacement maps is the primary goal of this work, we emphasize that another important issue of the SISTEM

methodology is to provide the strain tensor components ($\varepsilon_{11}\ \varepsilon_{12}\ \varepsilon_{13}\ \varepsilon_{22}\ \varepsilon_{23}\ \varepsilon_{33}$) and the body rotation tensor ($\omega_1\ \omega_2\ \omega_3$) .

For simplicity we show the three meaningful invariants of the 3D strain field [37]: the "dilatation", the "differential rotation magnitude" and the maximum shear strain" (see Fig.3). The dilatation is the only linear invariant and it is defined as follows:

$$\sigma = \frac{1}{n}\sum_{i=1}^{n}\varepsilon_{ii} \tag{14}$$

where ε_{ii} are the diagonal elements of the strain tensor matrix (2). The differential rotation magnitude invariant is a quadratic invariant and it is given by the following expression:

$$\Omega^2 = \omega_1{}^2 + \omega_2{}^2 + \omega_3{}^2 \tag{15}$$

Finally the maximum shear strain is given by

$$M = \lambda_{\max} - \lambda_{\min} \tag{16}$$

where λ_{max} and λ_{min} are respectively the largest and the smallest eigenvalues of the strain tensor matrix (2).

The shape and magnitude of the three invariants are in agreement with the Mogi source adopted for this synthetic case.

A further aim of the synthetic test is to investigate the distribution of RMSE as a function of the number of EPs considered in the range of 12 to 150. In order to assess from the statistical point of view the RMSE we have performed an appropriate number of simulations. In particular we have considered the following sequence of points: 12,20,30, … , 140, 150. For a fixed number of EP we have randomly generated 5000 different configurations of EP in the rectangular domain considered and evaluated the corresponding locality parameter d_0. This means that for a fixed number of EPs a range of values is obtained as show in Fig. 4. As obvious for increasing number of EP both the range and the mean values of d_0 decreases.

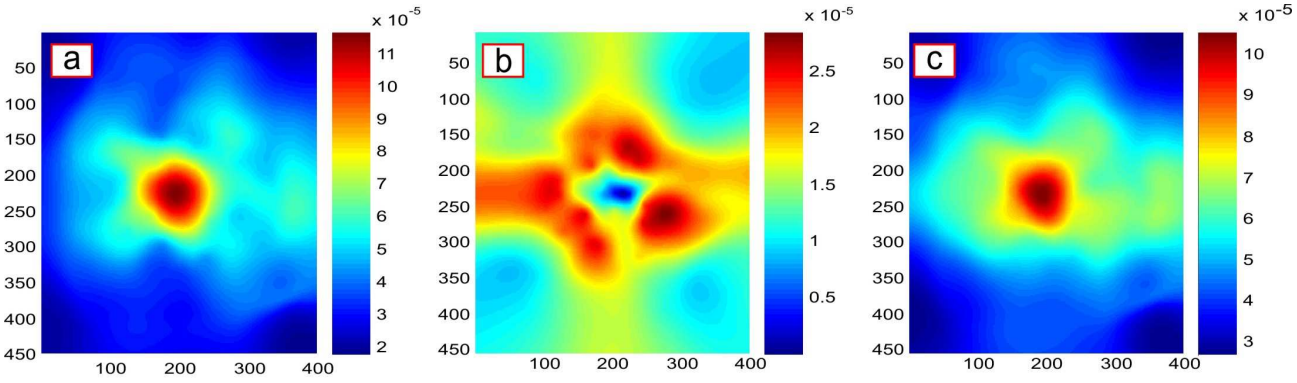

Figure.3 Strain invariants for the synthetic case study. The "dilatation" (a) , the "differential rotation magnitude" (b) and the maximum shear strain"(c). All quantities are dimensionless.

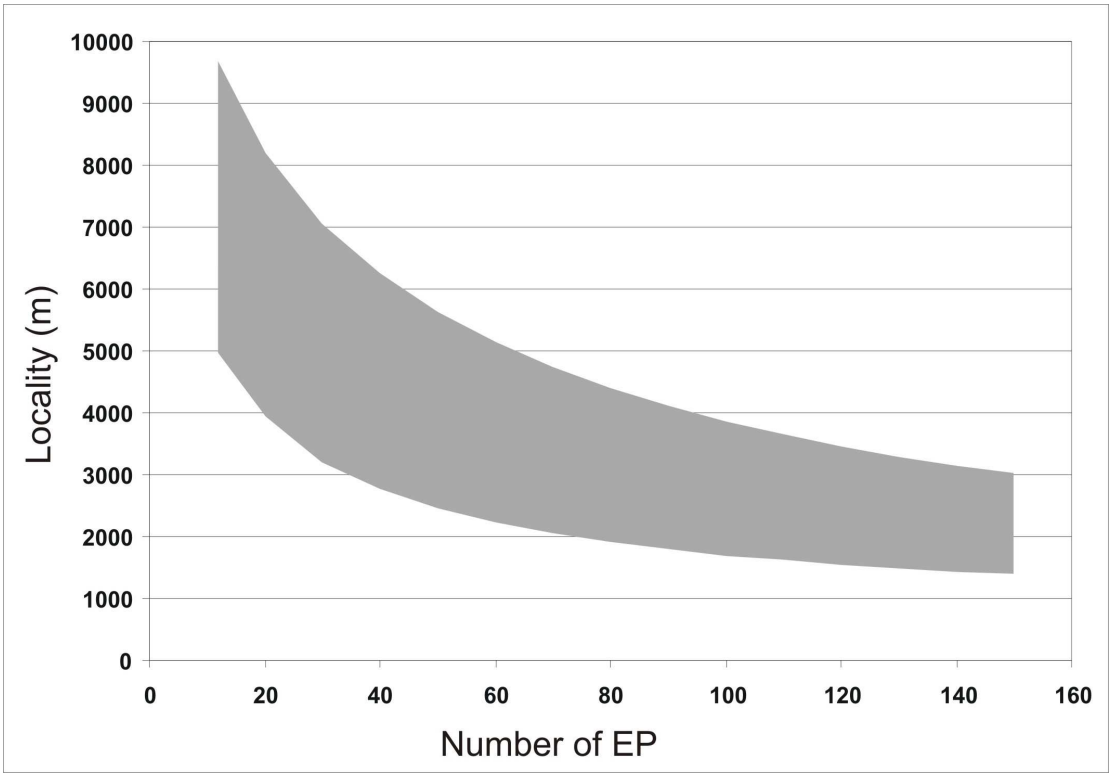

Figure.4 Locality (d_0) in meter vs. number of Experimental Points (EPs), for the synthetic case of study. The d_0 value is calculated using 5000 random configurations, for each number of EPs, on an area of 2000 Km^2, according to the equation (11).

The behavior of the RMSE vs the number of EP is reported in Fig. 5. It is possible to see that, as expected, the RMSE decreases (and thus the accuracy of the method increases) as the number of EP point increases. However the plateau visible in Fig. 5 suggests that in the considered synthetic case study a good trade-off between accuracy and number of EPs can be obtained by using 50-60 EPs. Indeed, for a number of EPs greater than 50-60 there are no significant improvement of the performance. We highlight that the magnitude of the RMSE are comparable with those reported by [9, 38].

One finding of this test is that the vertical component has, in general, accuracies better than the horizontal ones. This result was somehow expected, bearing in mind that the DInSAR images have an average vertical directional cosine of about 0.90 and therefore are particular sensitive to vertical movements.

Furthermore we have characterized the dependence of the errors of each component of the obtained 3D displacement map as a function of the DInSAR error, as proposed by [38]. Fig. 6 shows the results of the dependence of the error as function of the DInSAR error, assuming 70 EPs randomly located. There is a marked influence of the DInSAR error variance in the Up components whereas the East and North components seem insensitive to the noise level. This is another confirmation of the effect of the sensitivity of the DInSAR to the Up component of the deformations.

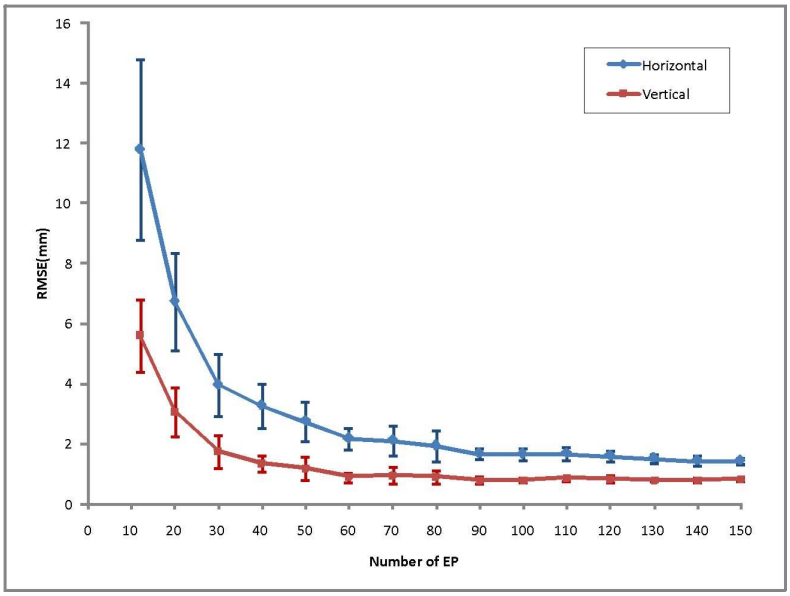

Figure.5 Mean RMSE vs. number of EP. In blue and red the mean RMSE for the horizontal and vertical components are reported respectively. For each dataset is reported the corresponding standard deviation .

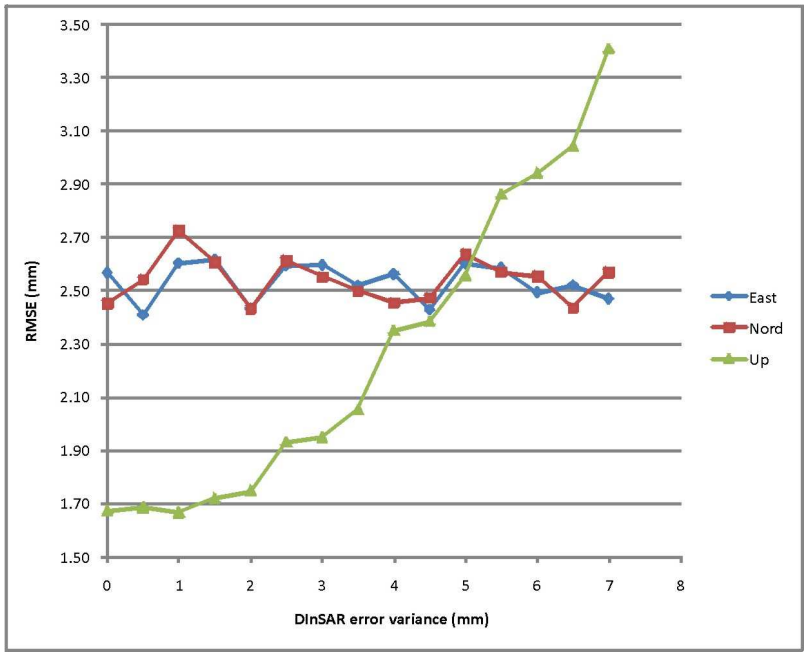

Figure 6. Variation of the optimized displacements errors vs. the DInSAR errors for the synthetic case of study

A real case study performed on the Mt Etna area

In this section, we apply the SISTEM method to compute 3D high-resolution surface displacement maps of Mt. Etna related to ground deformations observed by GPS and InSAR in the period 2003-2004.

The GPS data used in this work refer to July 2003 - July 2004 period and were analyzed and modeled by [39]. This GPS dataset shows a significant inflation affecting the western and upper flanks, with a maximum of about 5 cm located on the upper southern flank, coupled with an eastward movement of the benchmarks located on the eastern flank of the volcano (Fig. 7).

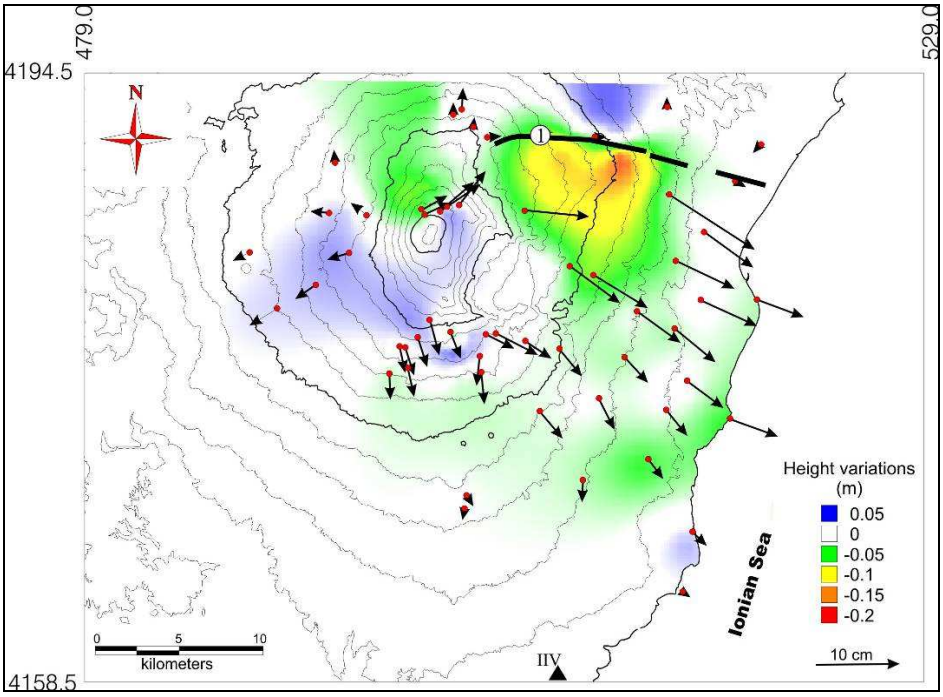

Figure 7. Displacement vectors and height variations from the comparison between July 2003 and July 2004 (redrawn from [39]). The arrows represent the horizontal displacement vectors, while the vertical displacement is presented by a contouring of color fringes obtained by interpolating the measurements relevant to each benchmark. In the map is reported the schematic geometry of the Pernicana fault system (1). The triangle represents the location of IIV station.

In order to integrate the GPS and the DInSAR data, an appropriate pair of ascending ERS2 SAR images was selected; they refer to the 20 August 2003 to 30 June 2004 interval and have a 70 m of perpendicular baseline (which produces a height of ambiguity of about 126 m). This interferogram was processed using the Jet Propulsion Laboratories (JPLs)/Caltech Repeat Orbit Interferometry Package (ROI_PAC, version 3.0). Fig. 8 shows the corresponding displacements map in LOS, obtained by unwrapping the interferogram.

In order to have the two dataset (i.e. GPS and DInSAR) temporally consistent, we scaled the observed values under the assumption of a linear evolution of the ground deformation pattern through time. It means to assume a simple principle of yearly partitioning, by scaling the DInSAR data to the time span of the GPS dataset (12 months). The GPS ground displacements refer to the IIV station (located on the city of Catania (fig. 7), which was assumed as fixed from 2003 and 2004. Since the interferogram has no absolute reference datum, we shifted the LOS displacements in order to tie it to the IIV station. Furthermore, we resampled the LOS displacements into a regular grid 400x450 with a pixel size of 100 meters (Fig. 8).

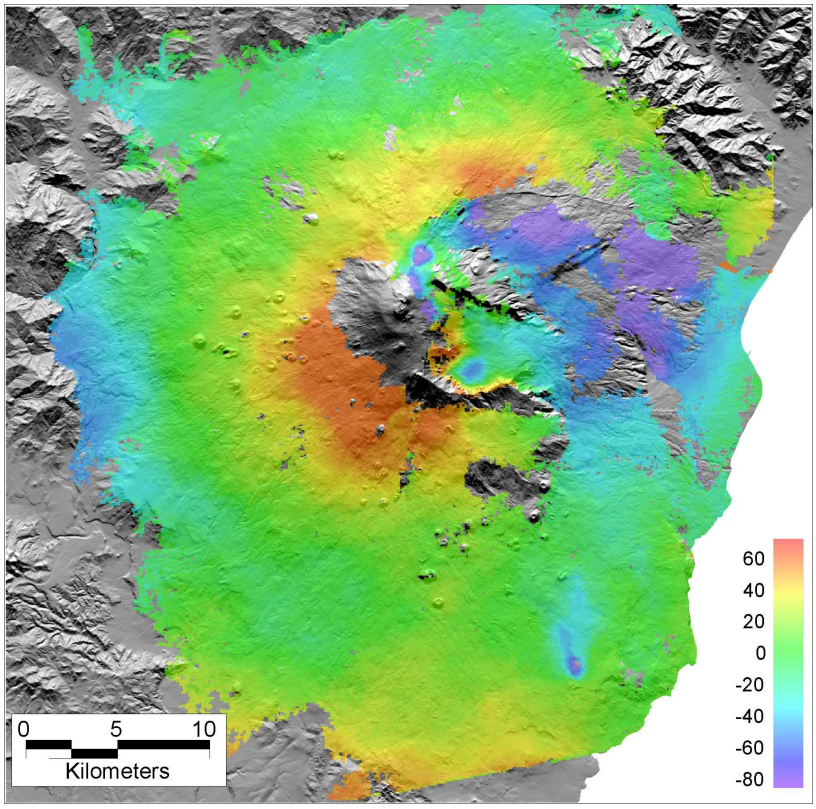

Figure 8. Resampled Line of sight (LOS) displacement map in millimeters, calculated for the unwrapped interferograms relevant to the ERS2 ascending pair 20 August 2003 to 30 June 2004.

Fig 9(a)-(c) show the results of the integration through SISTEM of the GPS and DInSAR data set reported in Fig. 7 and Fig. 8, by assuming d_0=1500; the corresponding estimated standard errors are shown in Fig. 9(a)-(c).

According the knowledge of the volcanic activity of the volcano through this period and the results of the previous studies [39], two main phenomena characterize the dynamic of the Mt. Etna between the July 2003 and the July 2004: the recharging of the deep plumbing system centered below the upper western flank [40] (at about 3-8 km b.s.l.) and the ESE sliding of the eastern and southeastern flank (the faster measured during the last decade). Thus, in the results of SISTEM, we expect to find the effects of these phenomena.

The East component map shows an evident displacement of the eastern flank of Mt. Etna bounded northward by the Pernicana fault system (see fig. 7) as expected form the ESE sliding of the north-eastern flank [41], while on the whole western flank SISTEM measure westward movements, due to the effects of the deep magmatic sources [40]. The ESE sliding of the eastern flank is also evident on the North component of the south-eastern flank, as a negative value, while on the northern and the on the whole western flank the North-South component shows clear evidence of deformation due to the deep magmatic sources. The most evident vertical movement (uplift) is localized in the summit western area according with the recharging phase of the plumbing system of the volcano identified by [39]. This excludes that the high LOS displacements observed in Figure 8 can be attributed to topographic and/or atmospheric effects, as it might be suggested by considering the interferogram alone.

All these features are hence compatible with the dynamic of the volcano during the investigated period [39].

The estimated standard error maps of the horizontal components (figures 9a' and 9b') have similar patterns each other while that relevant to the vertical component (figures 9c') is different.

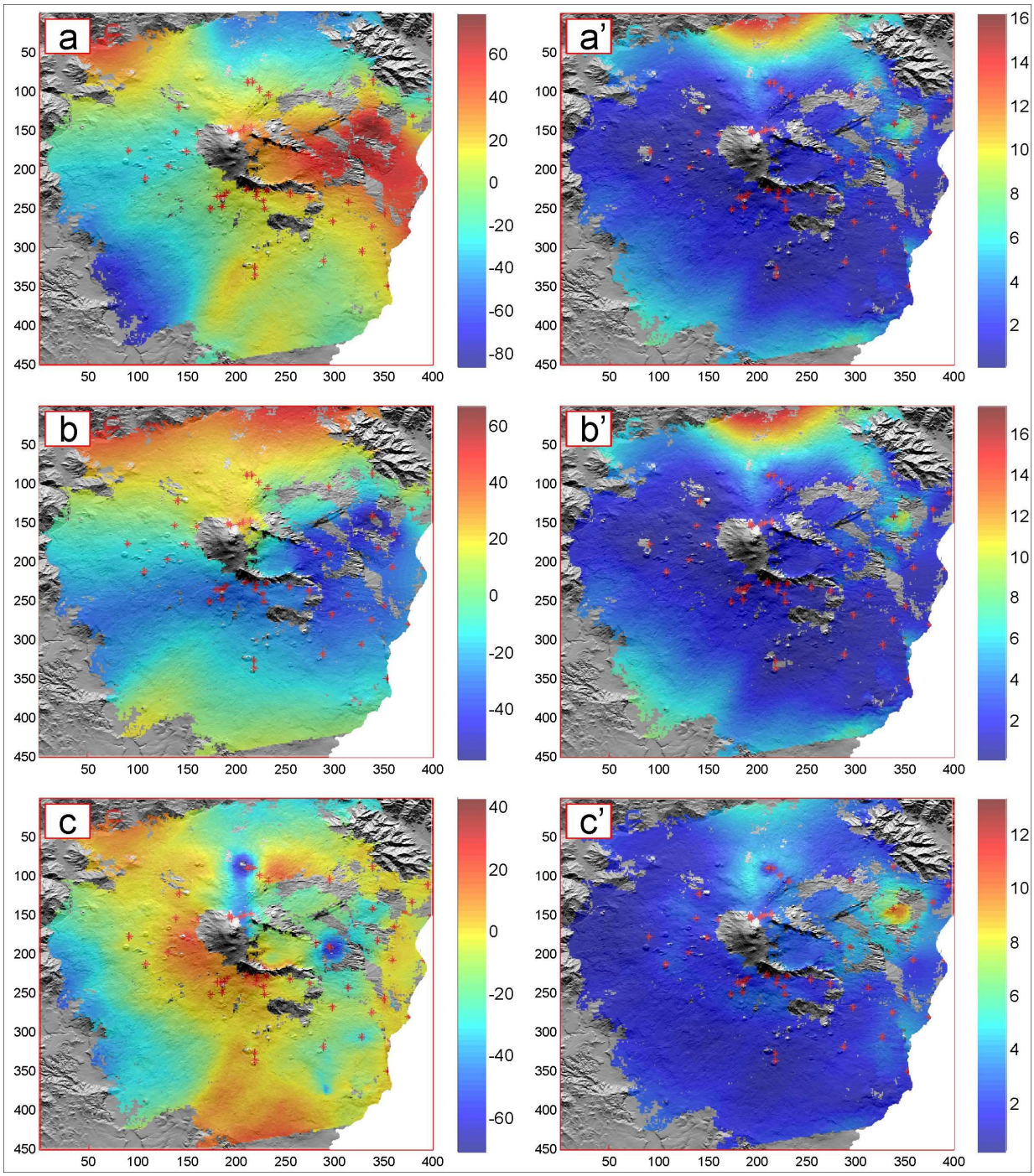

Figure 9. GPS and DInSAR data integration results. In the frames (a), (b), and (c) are reported the calculated East, North and Up components of displacements respectively. In the right column the

corresponding estimated standard errors of East (a'), North (b') and Up (c') components are reported. The red crosses represent the GPS stations.

Furthermore, we observe that the magnitude of the vertical errors are, in general, lower than those of the horizontal components. In order to explain these results, which conform with those relevant to the synthetic test, we have to consider that the estimated standard errors provided by the SISTEM come out from an optimization process (i.e. the WLS). This means that both observations and covariance matrices play a role in estimating them. Thus the figures 9a', 9b' and 9c' may be explained bearing in mind that: i) the variance of the DInSAR data is a scalar, thus it weights the three components with the same value; ii) the variances of the East and North components of GPS data are similar, thus they give similar contributions to the corresponding estimated error maps (9a' and 9b'); iii) the DInSAR data is more sensitive to the vertical deformations thus it reinforces the estimation of the vertical component, reducing the magnitude of the vertical estimated standard error (figure 9c').

A direct comparison between the GPS components and the components estimated by applying the SISTEM method is here provided (Figure 10).

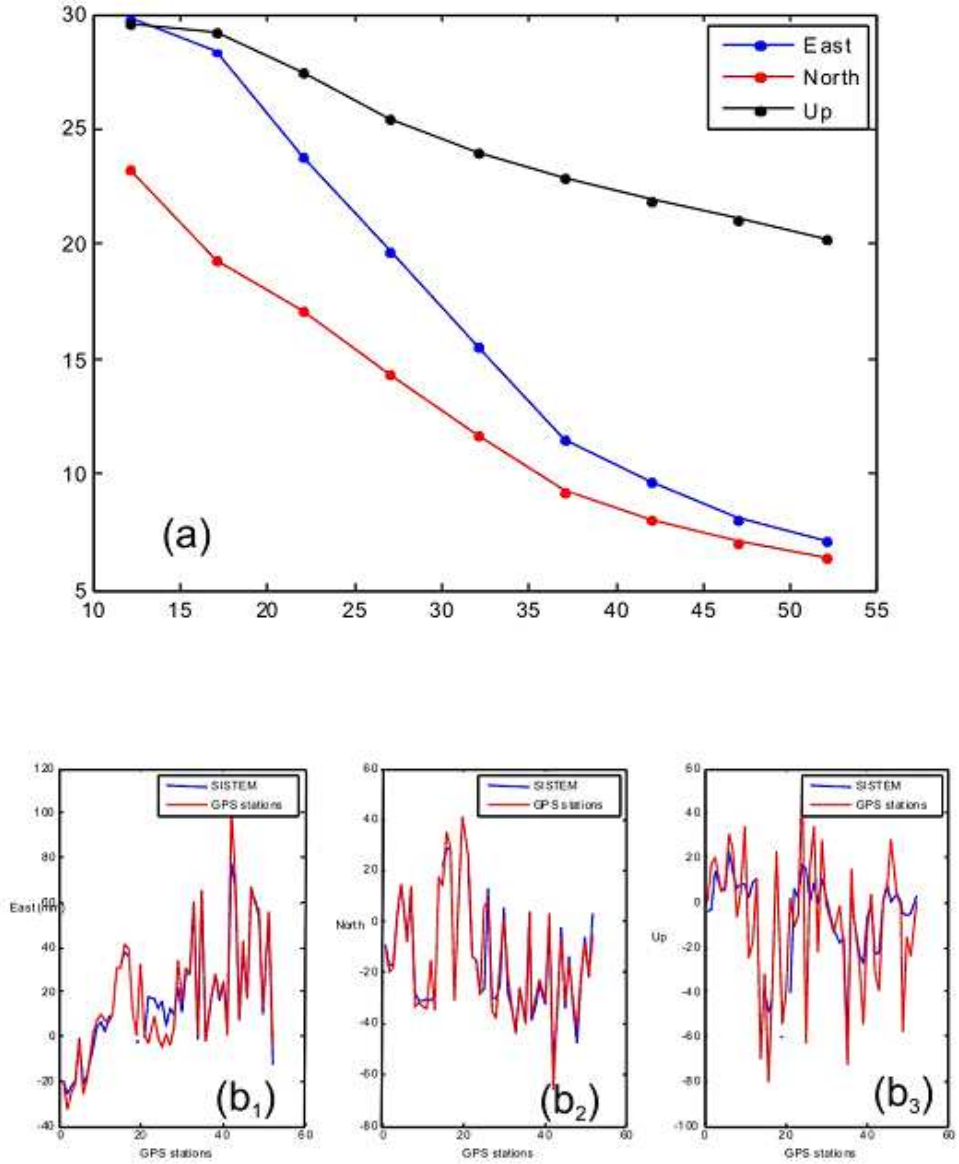

Figure 10. a) RMSE (in mm) between the SISTEM output and the GPS data calculated at the GPS site locations as a function of the number of GPS stations; b_1), b_2) and b_3) show the values of the discrepancy relevant to the East, North and Vertical components respectively, computed for the whole network configuration (i.e. 52 GP stations).

The purpose of this comparison is twofold: to characterize the accuracy of the SISTEM approach as a functions of the number of GPS points, and to evaluate how the combined DInSAR+GPS components differ from the GPS components alone.

In order to carry out this comparison, we perform several runs, by increasing the number of GPS points from 12 to 52. For each number of GPS points, we performed 100 numerical simulations, so that we consider 100 different sub-networks, each configuration randomly chosen within the whole GPS network, in order to asses a statistically significant mean RMSE. In these tests, the RMSE is computed at the site locations of the whole GPS network (i.e. 52 points) by comparing the SISTEM output and the measured deformations.

Figure 10a shows that, in general, the RMSE decreases as the number of GPS stations increases, confirming the results of the synthetic test (compare Fig. 4). In particular it is possible to appreciate that by increasing the number of GPS points from 12 to 52 the RMSE decrease of about 1.0, 1.6 and 2.3 cm respectively for the Up, East and North components. The main difference with the synthetic test is that the discrepancy measured by using actual GPS data is higher for the vertical component than for the horizontal ones. This is due to the fact that, differently than the synthetic data, actual GPS data suffer of a low accuracy in the vertical component. Fig. ($10b_3$) clearly indicates that SISTEM "correct" the GPS Up components much more than the East and North components (Figure $10b_1$ and $10b_2$). Furthermore, this analysis shows that the integration of the DINSAR and GPS data affect more the East than the North component, since the discrepancies between SISTEM and original GPS are negligible for the North component (Figure $10b_2$) while some variations are appreciable for the East component (Figure $10b_1$).

All these results highlight the role of the DInSAR data in the integration and, in general, the tradeoff between DInSAR and GPS data in the integration method, the former influencing

much more the components where the latter is “weak” and vice versa. This is certainly due to the intrinsic capability of the WLS to compensate the original measurements and confirm that the aim to exploit the complementary nature of the GPS and DInSAR measurements is fully achieved.

Chapter 3

Modeling

Introduction

We present a strategy aimed to modeling large data set of 3D complex ground deformation patterns obtained by integrating sparse Global Positioning System (GPS) measurements of deformations and Differential Interferometric Synthetic Aperture Radar (DInSAR) maps of movements of the Earth's surface through the SISTEM method. In order to find the optimal model a Particle Swarm Optimization (PSO) algorithm is first used to locate optimal regions of complex search spaces. Then a derivative-based method, in particular the Gauss-Newton one, is used to refine results. The proposed strategy was tested on synthetic datasets in order to assess the performance. Furthermore it was used to model the 3D ground displacements map derived by integrating GPS and DInSAR data carried out on the Abruzzo region during the 2009 earthquake.

An Inverse Modeling method based on Particle Swarm Optimization

The problem of inverse modelling consists of estimating source geometry from the observed surface displacements. Surface displacements d can be related to the source geometry by a function g of the source model parameters m:

$$d = g(m) + \varepsilon \qquad (1)$$

where ε is the vector of observation errors.

We use a two steps inversion approach in order to find the optimal source model m^* related to the 3D ground deformation map provided by the SISTEM method. In particular we first use a PSO algorithm [42] in order to locate the valleys that contain the best models; then a derivative-based method, the Gauss-Newton one, is used to reach the bottom of each valleys in order to determine the optimal source model that minimize the misfit between 3D ground deformation map and prediction.

PSO is an iterative-heuristic, population-based global search algorithm used for optimization of continuous nonlinear functions. It models the social behaviour of bird flocking or fish schooling in the attempt to converge to the global optimum. PSO works with a population of interacting particles. Each particle is defined within the context of a topological neighbourhood comprising itself and some other particles in the population. Each particle moves in the parameter space with an auto-adaptive velocity whose value depends on the move experiences of its own and those of its companions. In particular each particle remembers both its best previous position $p_i=(p_{i1}, p_{i2}, \ldots, p_{iD})$ and the neighbourhood's best position $p_g=(p_{g1}, p_{g2}, \ldots, p_{gD})$. In this work the particle positions are manipulated according to the following equations:

$$v_{i+1} = C\left(v_i + c_1 r_1 (p_i - x_i) + c_2 r_2 (p_g - x_i)\right) \tag{2}$$

$$x_{i+1} = x_i + v_{i+1} \tag{3}$$

where the position and the velocity of the i^{th} particle are represented respectively as $x_i=(x_{i1}, x_{i2}, \ldots, x_{iD})$ and $v_i=(v_{i1}, v_{i2}, \ldots, v_{iD})$, c_1 and c_2 are two positive constants taking into account

respectively the influence of each particle's knowledge (cognitive parameter) and that of the whole swarm (social parameter). Parameters r_1 and r_2 are random number, which are chosen uniformly within the interval *[0, 1]*, used to add an element of randomness to the movements of the particles. Finally *C* is a constriction function used to limited the velocity values to a fixed range.

At each iteration the adopted objective function is evaluated for each particle position, the vector parameters p_i and p_g are update, the particle velocities are manipulated according to eq. (1) and (2) and an appropriate stopping criterion is checked. Detailed information are provided in [43-45].

In this work the PSO is basically used to find the optimal region of the parameters space, thus providing a set of good initial conditions for the Gauss-Newton derivative-based method that is used in the attempt to reach the global minimum. These initial conditions are represented by the best particle of each neighbour of the swarm. The advantages of using this strategy are that the PSO algorithms are very simple – their implementation requires few lines of code -, is able to localize very fast the optimal regions of the parameters space. Furthermore they provide a set of good initial guesses to the derivative-based method thus ensuring it good performance. Indeed it is well known that derivative-based methods work well only when the initial guess is near the global minimum.

In order to assess the performance of the proposed two steps approach we have carried out several inversion tests on synthetic dataset. In particular we have generated 3D ground deformation maps by using the Mogi [34] and the Okada [46] forward models within a 60x52 regular grid (cell-size 500 m x 500 m). To statistically evaluate the accuracy of inversion, 100 models with uniformly distributed parameters, whose values were fixed in ranges that resemble likely cases in volcanic area, were inverted. In order to asses the goodness of the

inverse modelling approach, the Mean Absolute Percentage Error (MAPE) was calculated for each model parameter P_{Ci} :

$$MAPE_i = \frac{1}{N}\sum_{i=1}^{N}\left|\frac{P_{Ci} - P_{Ti}}{P_{Ci}}\right| \quad (4)$$

where N is the number of the considered models, P_{Ti} is the generic ith parameter of the calculated model and P_{Ci} is the corresponding true parameter.

For all inversion problems, as first step, we have used a population of sixty agents subdivided in three groups of twenty. Then the Gauss-Newton method was run with initial guess being, respectively, the best agent of each group.

We have found a very low *MAPE* index for all the model parameters (less than 1 per cent) thus ensuring the suitability of the proposed inversion strategy.

The Abruzzo earthquake case study

In order to perform the inversion modeling of ground deformation observed in the Abruzzo region during the 2009 earthquake, both GPS and DInSAR data were preliminary integrated by using the SISTEM method in order to derive 3D ground deformation map over the whole investigated area. GPS data were provided by the Centro Nazionale Terremoti. DInSAR interferograms were processed by the ROI_PAC 3.0.1 software developed by Jet Propulsion Laboratory/California Institute of Technology .

This is a very interesting application of the SISTEM method, indeed three different interferograms respectively AlOS (fig. 1), Envisat ascending (fig. 2) and Envisat descending (fig. 3) are simultaneously integrated with GPS data.

Thanks are due to the ESA, which made quickly available the satellite images just after their acquisition in the framework of the Earth Watching project. We have produced the ascending and descending Envisat interferograms that show the ground deformation due to the earthquake. In particular we have produced the Envisat-descending Interferogram refers to 27/04/2008 – 12/04/2009 (t_{bline} = 350 days; B_{perp} = 44 m) and the Envisat-ascending Interferogram refers to 11/03/2009 - 15/04/2009 (t_{bline} = 35 days; B_{perp} = 227 m). Furthermore an ALOS PALSAR interferogram produced with images acquired along the 638 ascending tracks and relevant to the 3/7/2008 - 21/5/2009 time interval (tbline = 322 days; Bperp = 665 m) was processed.

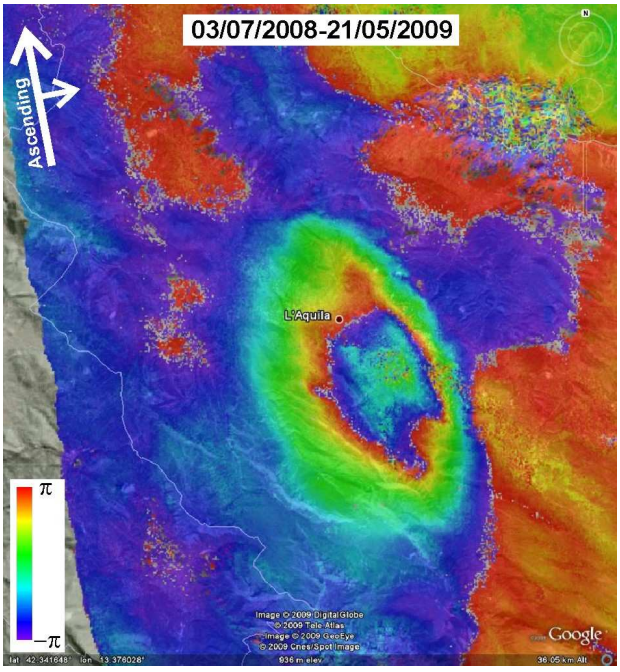

Figure 1. ALOS PALSAR interferogram.

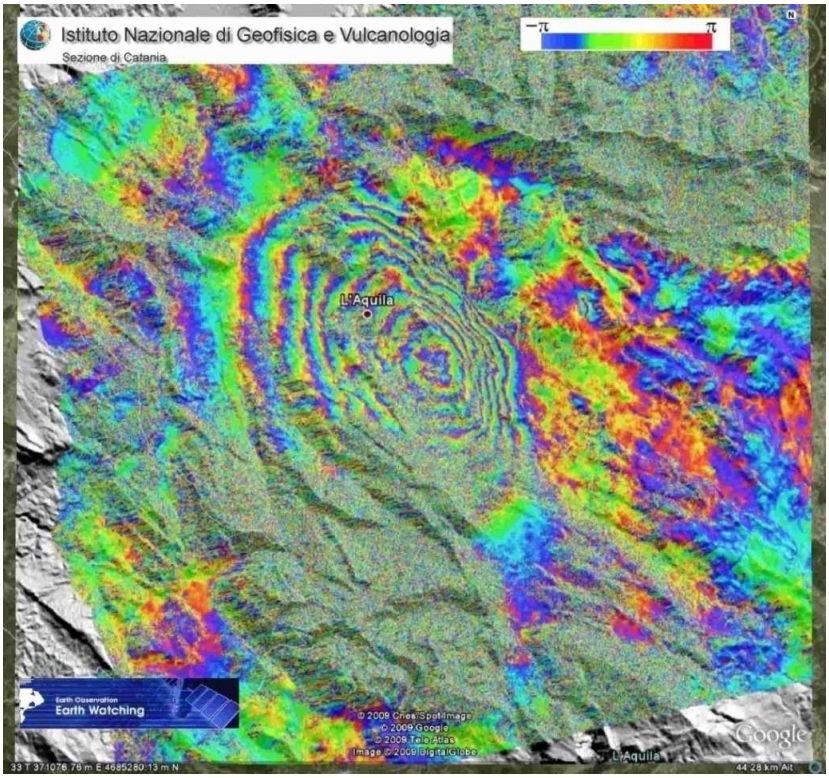

Figure 2. Envisat-Descending interferogram.

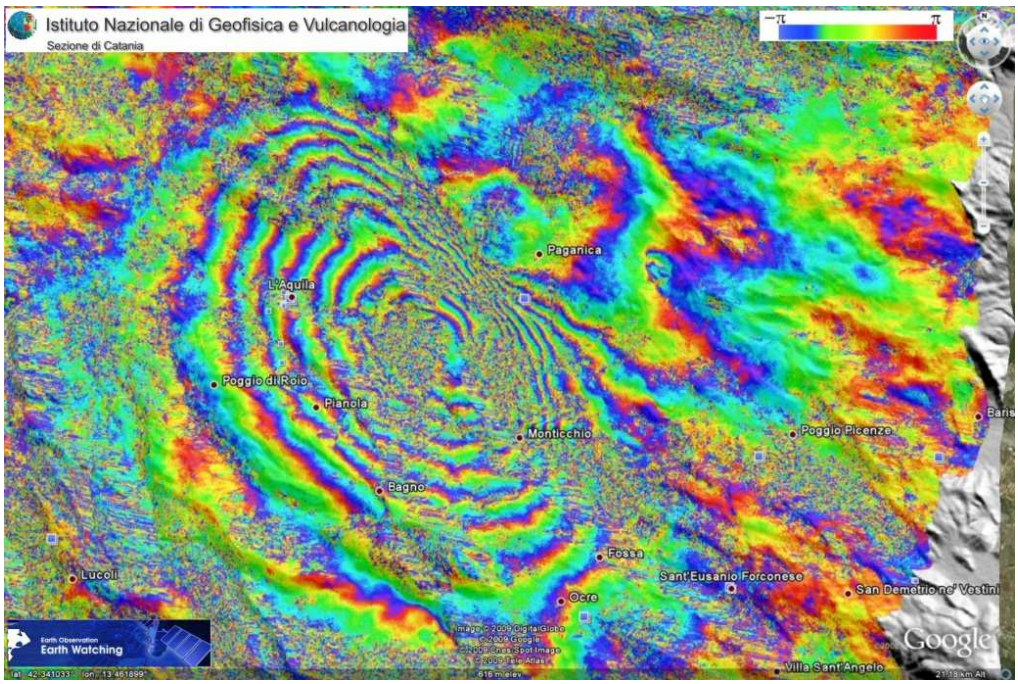

Figure 3. Envisat ascending

In order to achieve high accuracy three-dimensional surface motion maps, related to the L'Aquila earthquake, we have exploited the standard formulation of SISTEM approach, taking in account DInSAR data with ascending and descending geometry (fig. 4).

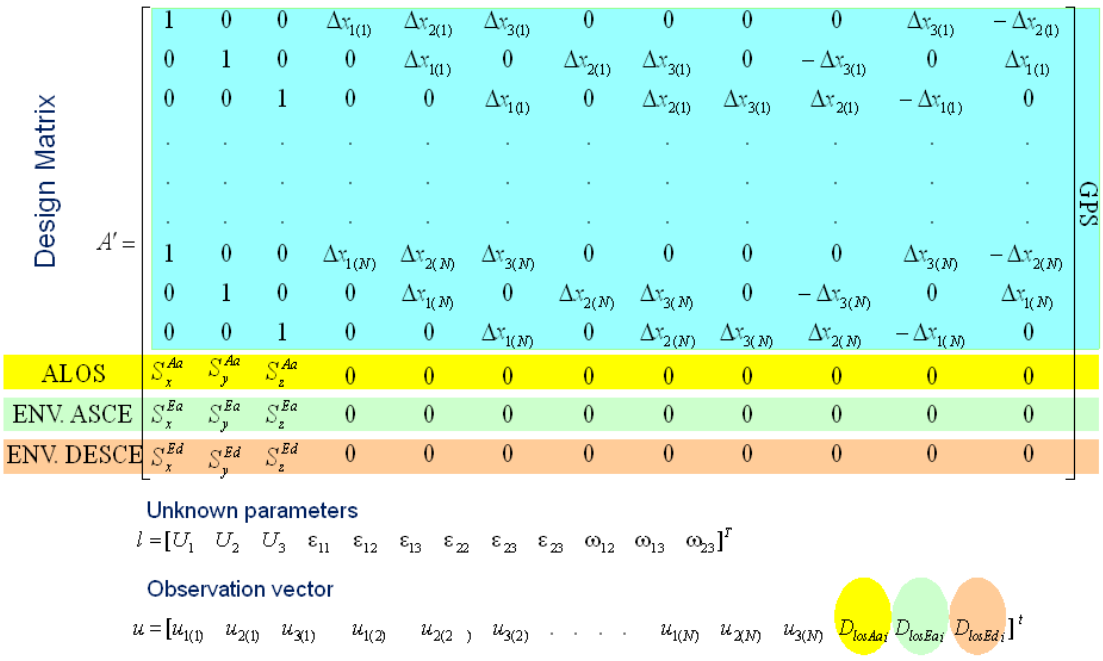

Figure 4. SISTEM formulation combining GPS data and three interferograms.

The results of the SISTEM method (fig . 5) show that the reconstructed deformation pattern is compatible with the surface evidences of the Paganica fault system, whit a mainly Dip-Slip (Dh max =- 22 cm ± 1cm) and a minor dextral movement of the fault system.

The 3D displacements map derived by the SISTEM method was used to estimate the source geometry. We assume that the fault can be approximated with dislocation in a homogeneous elastic half-space [46]. The adopted cost function is the following Root Mean Square Error (RMSE)

$$J = \frac{1}{N}\sum_{i=1}^{N}\left(\frac{1}{\left(w_i^x\right)^2}(O_i^x - P_i^x)^2\right) \quad (5)$$

where $x=\{East, North, Up\}$, O_i^x and P_i^x indicate the observed (SISTEM integration result) and the simulated values respectively and the terms w_i^x represent the estimated standard errors provided by the SISTEM method.

In table 1 the estimated parameters are reported. These parameters are in agreement both to the kinematic and to the geological evidences of the Paganica fault system with a mainly dip-slip component and dextral strike-slip.

Depth	*5144 m*
Strike	*132 gradi*
Dip	*67 gradi*
Length	*11970 m*
Width	*13000 m*
Strike-slip	*-0.04 m*
Dip-slip	*-0.9 m*
Opening	*0.2 m*
Xs	*37487385*10^6*
Ys	*4.6877719*10^6*

Table 1. Estimated parameters values

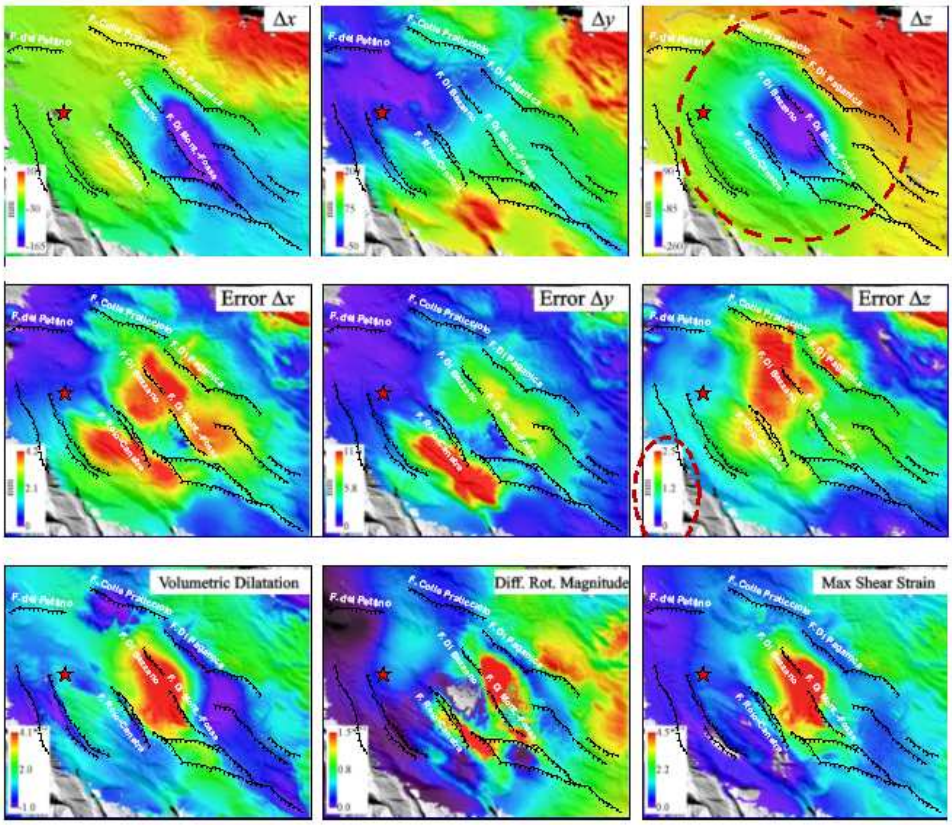

Figure 5. In the first row are reported respectively the East, North and Up ground deformation map. In the second row the relevant estimated standard errors are reported. Finally the volumetric dilatation, the differential magnitude and the max shear strain are shown.

Chapter 4

Toward a more realistic volcanic source shape

In geophysical science choosing an analytical or numerical model in order to gain a better understanding of the observed surface displacements is usually based on a preliminary visual inspection of the ground deformation patterns. Indeed the model-maker, based on its own experience gained in the inversion modeling framework, is usually able to presuppose and associate a model to a particular ground deformation pattern. Then an optimization algorithm is used to estimate the source geometry parameters.

In this chapter we propose an automatic method based on Artificial Neural Networks (ANN) in order to provide a valid support to the choose of the source model. In particular, given a 3D ground deformation pattern the ANN is used in the attempt to build the relevant three dimensional volcanic source shape in the discrete Euclidean space. The methodology was tested both on synthetic and real datasets.

Introduction

In geophysics the problem of estimating the source parameters from the observed ground deformation data is known as inverse modeling. It is a very important task and attract the interest of many researchers. The inverse modeling problem requires the assumption of an analytical or numerical forward model. This model is basically chosen based on the experience of the model-maker. Indeed a crucial step in the inverse modeling problem is the visual inspection of ground deformation patterns in order to select the theoretical forward model that in a more reliable way will be able to fit the observations. In the attempt to emulate this kind of human thought process by a soft-computing technique, an approach based on the

Artificial Neural Networks (ANNs) is proposed. The aim of this study is to show that given a generic 3D ground deformation pattern due to a source pressure, an opportunely trained ANN is able to build the relevant three dimensional source shape. Furthermore will be emphasized the ability of the ANN to generalize this association for both single, multi sources and source pressure model different from those used during the learning phase.

In order to derive 3D ground deformation pattern over the whole investigated area the SISTEM was used. A brief introduction to the artificial neural network is given. Then the methodology and the first preliminary results achieved on synthetic datasets are reported; Finally a real case study and the conclusions of the methodology are reported.

Artificial Neural Network background

Artificial Neural Networks (ANNs) due to its learning and generalization capabilities are widely used in several fields of science and engineering. These interesting features make them an attractive tool for application to some geophysics problems. In particular an important application of ANNs has been the solution of geophysical inverse problems. Some examples reported in literature are the location of subsurface targets from electromagnetic field data [47], the inversion of seismic waveform data [48, 49]´and the integrated inversion of geophysical data of different types [50].

Roughly speaking an ANN can be described as a nonlinear function aimed to provide a mapping between known input–output patterns for a given problem. Consider a nonlinear input-output mapping described by the functional relationship:

$$d = f(x) \tag{1}$$

where x and d are the input and output vectors, respectively. The vector-valued function f() can be considered to be unknown, but it is assumed that a set of pairs (x_i,d_i), referred to as examples in typical neural network terminology, describing our knowledge about the function f() are given. A typical way of approximating static system using the popular single-hidden-layer multilayer perceptrone (MLP) [51-53] is the following:

$$y_k(x) = \sum_{j=1}^{NH} c_j \varphi(\omega_j^T \cdot x + t_j) + c_0 \tag{2}$$

where $y_k(x)$ is the *kth* entry of the approximated function, $\varphi()$ is a sigmoid function (i.e., $\varphi(z)=1/(1+e^{-\alpha z})$, x is the input vector, ω_j is the vector of coefficients, c_j and t_j are additional adjustable coefficients.

The approximation problem has an inverse that consist of constructing a system that produces the vector x in response to the vector d. The inverse system may thus be described by

$$x = f^{-1}(d) \tag{3}$$

where the vector-valued function denotes the inverse of f. The theoretical aspects concerning the use of MLPs for function approximation lie on the so-called Universal Approximation Theorem [54], which can be invoked to prove that an MLP with a single hidden layer is sufficient to compute a uniform approximation to a given training set represented by the set of inputs $(x_1, \ldots ,x_m)$ and a desired (target) output $f(x_1, \ldots ,x_m)$ with a prefixed degree of accuracy.

The problem we want to solve by using the ANNs is to build the source shape of a pressure source in a Euclidian discrete space given the relevant ground deformation pattern. This

problem can be formulated in the following manner. Let *P* be a generic pressure source shape and *D* the associated ground deformation pattern. As the shape *P* varies a different pattern *D* is obtained. This concept can be expressed in symbol form as

$$f(P) \rightarrow D \tag{4}$$

Using (x), which is known, it is therefore possible to produce a population of pairs *(d,P)* that represent the whole "data space" observed. This population will be used as the training set for the neural network.

Building the source shape on the basis of the data observed using a neural approach thus means finding an approximated function of the inverse of (4), as indicated in (5)

$$f^{-1}(D) \rightarrow P \tag{5}$$

It should be remarked that, to approximate a function using multilayer perceptron (MLP) ANNs and ensure that the approximation error is bounded, it is necessary to assume that the function to approximate exists and is both continuous and smooth. However, it is evident from the equations of the mathematical model used here (Okada–Murakami–Fittermann–Ehrismann), that this is not easy to prove. To obtain some indications, it was considered useful to "test" the inverse function using numerical techniques of proven accuracy and robustness in the inversion of geophysical data such as the SA optimization method [55,56]. However, it is necessary to stress that it is just an indication, not analytical proof.

Methodology

The goal of this work is totally focused on the source shape investigation. In particular the aim of this paper is to reconstruct a 3D estimation of the source shape based on ground deformation observations. We stress here the difference between this approach and the traditional inverse modeling problem. The former tries to build a reliable shape source in a Euclidean discrete space, the latter is aimed to find the optimal parameters of *a priori* chosen source model.

To reach our goal an ANN was opportunely trained in order to learn the relationship between a given ground deformation pattern and the relevant 3D source shape. The dataset used for the training phase has been generated by using the finite spherical pressure source model [57]:

$$\begin{pmatrix} u \\ v \\ w \end{pmatrix} = \left(\alpha^3 \Delta P \frac{(1-\upsilon)}{G} \left(\left(1 + \left(\frac{\alpha}{d} \right)^3 \left(\frac{1+\upsilon}{2(-7+5\upsilon)} + \frac{15d^2(-2+\upsilon)}{4R^2(-7+5\upsilon)} \right) \right) \right) \right) \begin{pmatrix} \frac{x}{R^3} \\ \frac{y}{R^3} \\ \frac{z}{R^3} \end{pmatrix} \quad (6)$$

where *u*, *v*, *w* are displacements at the point *(x,y,0)*, *c=(0,0,-d)* and α are respectively the centre and the radius of the sphere, $R = \sqrt{x^2 + y^2 + z^2}$ is the radial distance from the centre of the sphere to a point on the surface, *ΔP* is the pressure change in the sphere, *G* is the shear modulus and υ is the Poisson's ratio.

The inputs of the ANN consist of the North, East and Up displacement components of each point of the investigated area. 1000 input patterns, i.e. 1000 3D ground deformation map each of which being a *20x20* pixels grid, have been generated with uniformly distributed parameters whose values were fixed in ranges that resemble likely cases in volcanic area.

In order to build the source shape each output O_i of the ANN is associated to a point $P(x_i,y,z_i)$ of the Euclidean discrete space. The output O_i is set to "1" if the corresponding point belongs to the source shape, "0" otherwise. Obviously the spatial resolution affect both the number of the outputs and the accuracy of the shape. A good trade-off is needed.

According to the finite spherical shape of the McTigue model, the output patterns have been prepared by using the following equations:

$$\begin{cases} P(x_i, y_i, z_i) = 1 \quad if \quad (x_i - x_0)^2 + (y_i - y_0)^2 + (z_i - z_0)^2 \le \alpha^2 \\ P(x_i, y_i, z_i) = 0 \quad if \quad (x_i - x_0)^2 + (y_i - y_0)^2 + (z_i - z_0)^2 > \alpha^2 \end{cases} \tag{7}$$

In figure 1 an example of input-output pattern is shown.

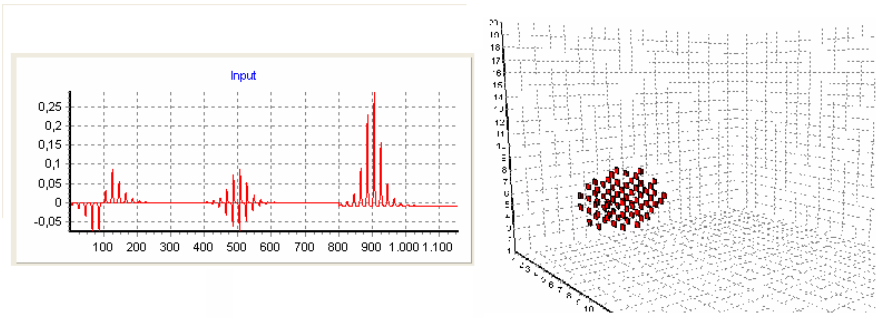

Figure 1. An example of an input-output pattern. The input pattern (left) consist on the displacement components of each point of the grid, East, North and Up respectively. The output pattern is the relevant 3D source shape reconstruction in a discrete Euclidian space.

The network was tested on a free noise synthetic dataset. In figure 2 results referring to a small, medium and big spherical source respectively are shown. It is evident that although the coarse grain space resolution of a 20x20x20 discrete Euclidian space the shapes reconstruction resemble spherical shapes in all three cases.

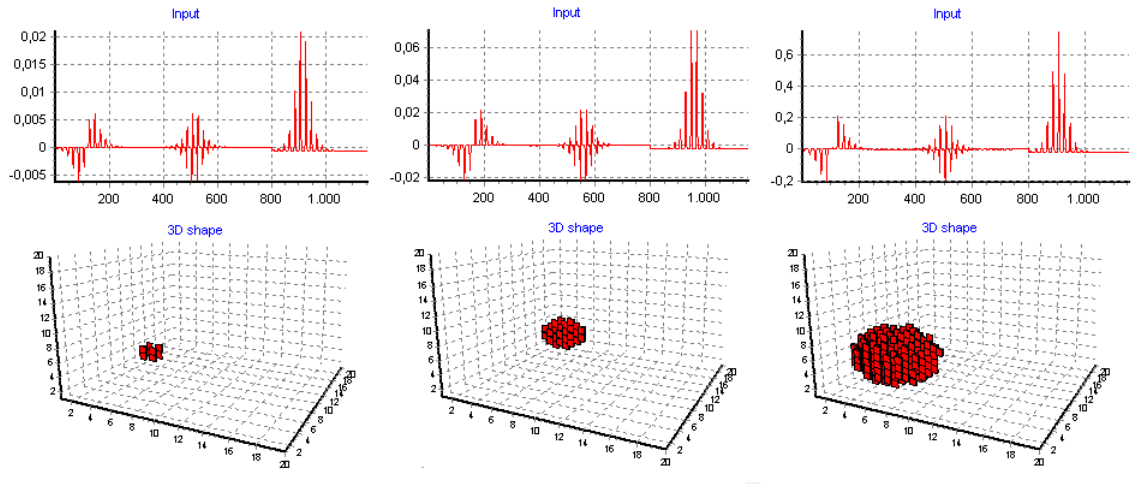

Figure 2. Reconstruction of a small, medium and big spherical source shape performed by the NN on the basis of their associated ground deformation patterns.

We have also tested the network with pattern deformation generated in a multi-source framework. In particular two and three spherical sources were considered. It was an experiment of great importance because the NN was not trained with this type of patterns, so it was a good test to investigate about the capability of generalization of the NN. Results relevant to two spherical sources are shown in figure 3. As we can see from this figure the NN was able to detect and reconstruct the two sources shape. The importance of this result is also emphasized by the nonuniqueness of the inverse geophysical problems. Indeed this neural network based approach provides *a priori* useful information (for example the volume) concerning the geometry of the sources into the inversion problem. This *a priori* information plays a key role in order to acquire a realistic and reliable solution.

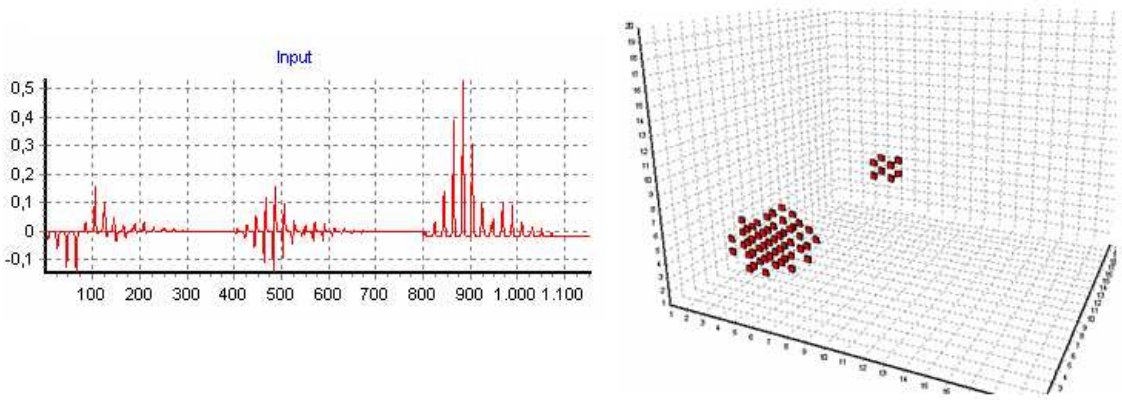

Figure 3. Input deformation pattern generated by two finite spherical sources pressure (left). Output reconstruction of the spherical source shape performed by the neural network.

We have also tested the network with several patterns deformation generated by an ellipsoidal pressure source [58]. Although the NN was trained by using only finite spherical source shapes, results had shown that it was able to reconstruct the ellipsoidal shape relevant to the ground deformation pattern derived by the Davis model. This was an ulterior considerable evidence of the capability of generalization of the NN. An example is reported in figure 4 where the reconstructed ellipsoidal-like shape is clearly visible.

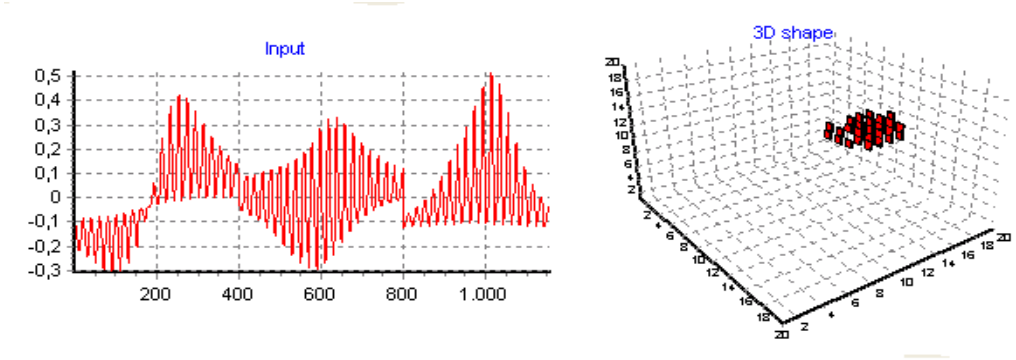

Figure 4. A test performed with a pattern deformation (left) generated by the Davis model. The output of the NN resembles the relevant ellipsoidal source shape.

Before showing a real application of the proposed technique (Sec. V), we briefly reports in the next section the method we have used in order to derive 3D ground deformation pattern from geodetic and satellite data.

Case study

In this section a real case study is reported. The proposed approach was applied on 3D ground deformation map of Mt. Etna derived by the integration of GPS and DInSAR data through the SISTEM method.

The GPS dataset used in this work refers to July 2003 - July 2004 period and was analyzed and modeled in [39]. This GPS dataset shows a significant inflation affecting the western and upper flanks, with a maximum of about 5 cm located on the upper southern flank, coupled with an eastward movement of the benchmarks located on the eastern flank of the volcano.

The DInSAR data was calculated on the basis of an appropriate pair of ascending ERS2 SAR images; they refer to the 20 August 2003 to 30 June 2004 interval and have a 70 m of perpendicular baseline (which produces a height of ambiguity of about 126 m). The relevant interferogram was processed using the Jet Propulsion Laboratories (JPLs)/Caltech Repeat Orbit Interferometry Package (ROI_PAC, version 3.0).

In figure 5 the East, North and Up components and their relative estimated standard errors derived by the SISTEM method are shown.

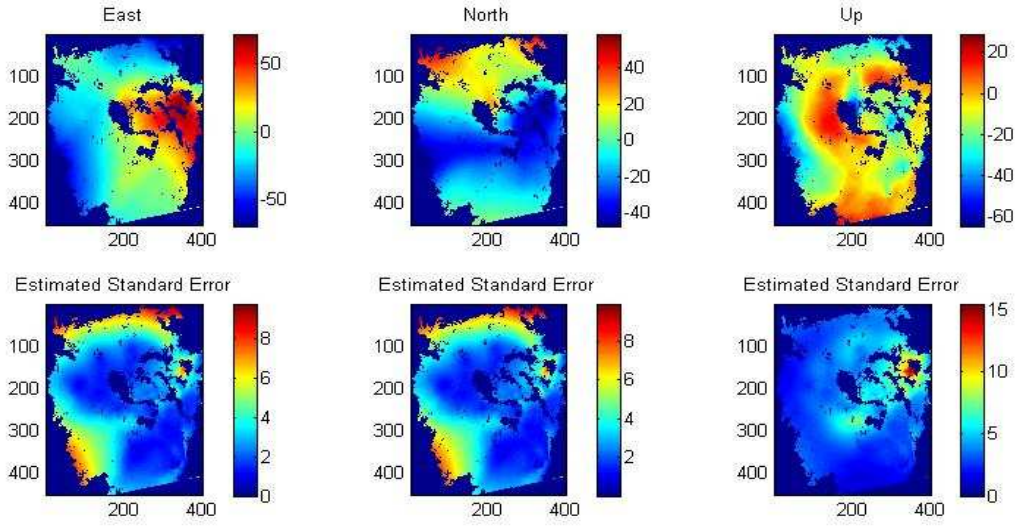

Figura 5. SISTEM results: East, North and Up displacement components (first row) and relevant estimated standard errors (second row).

As we can see in figure 5 the displacement data is not known in every point due to both geometrical aspects and low coherence affecting the SAR images. Therefore we have extracted a bi-dimensional binary mask from these maps (1 if there is the data, 0 elsewhere) in order to build the patterns to train the NN. After the NN was tested we have given the 3D SISTEM ground deformation map as input for the NN thus obtaining the volcanic source shape shown in figure 6. It is quite evident that the source shape suggested by the NN resembles something like a spherical shape located beneath the summit area. Such kind of source was used by [39] in order to model the significant inflation affecting the western and upper flanks. As we can see in figure 6 this method does not provided an ideal shape, rather a deformed shape, we think a more reliable source shape, processed based on both real ground deformation pattern and the knowledge gained from the NN during the learning phase.

The 3D ground deformation pattern derived by the SISTEM method is also affected by a marked eastward movement of the eastern flank of the volcano. The neural network was not

able to suggest a source shape associate to this pattern. Indeed such kind of ground deformation patterns are not due to sources pressure but they are attributable to dislocation faults [46]. Therefore it was an expected result that the NN trained solely with sources pressure generated patterns was not able to recognize a pattern due to a totally different mechanism, the fault dislocation one, from those the NN had been trained with.

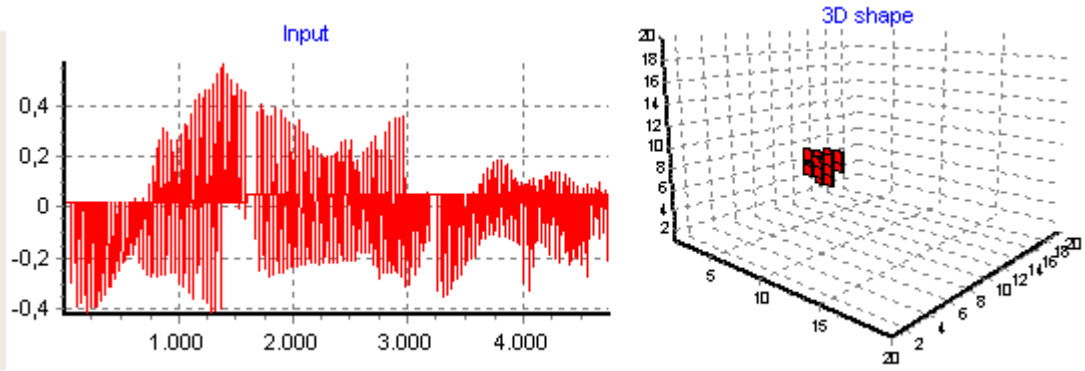

Figure 6. 3D ground deformation pattern derived by integrating GPS and DInSAR data in the period 2003-2004 (left); source shape estimation provided by the NN (right).

Conclusions

In order to derive three-dimensional surface motion maps, which take into account both sparse GPS measurements and DInSAR interferograms, a novel least square approach was proposed; the approach is named SISTEM as acronym of Simultaneous and Integrated Strain Tensor Estimation from geodetic and satellite deformation Measurements.

The novelty of the SISTEM method is that it is based on the elastic theory and that, with respect to previous methods known in literature, it does not require the preliminary step of interpolating sparse GPS measurements in order to fill in GPS displacements at the DInSAR grid but integrates them simultaneously.

In the proposed method, the mathematical relation between the unknown vector parameter (strain) and observation vector (displacements) is a matrix linear equation. Thus the estimation problem can be suitable solved by using the Weighted Least Square approach, hence avoiding complicated search schemes such as simulated annealing optimization algorithm. Since SISTEM is based on the small deformation theory, it provides the gradient displacements tensor estimation and the 3D component of the deformations within the entire investigated area.

First of all, SISTEM was tested on synthetic data simulating the deformations produced by a point pressure source below a volcanic-shaped topography. After having evaluated the capability of SISTEM to reconstruct the complete synthetic deformation field (i.e. the 3D plus the LOS displacements), these tests allow fixing a few main points concerning the use of this new approach, such as how to assess the locality parameter from the actual geodetic network configuration, the minimum number of GPS points beyond of which the accuracy do not change significantly (in the range of 50-60 in the considered domain, which in the synthetic

case in 40 km x 45 km) and the dependence of the final errors from the error of DInSAR data. The synthetic tests confirm that the final accuracy in terms of RMSE is in the order of 3-4 mm for the horizontal components and 2 for the vertical one, which are comparable with the performances of previous approaches having similar aims.

The proposed SISTEM method was then applied efficiently on the Mt. Etna area where the coverage of the GPS network is good and DInSAR data are available. The results (Fig. 9) show that the reconstructed deformation pattern conform with the geophysical and volcanological knowledge of the dynamic of Mt. Etna during the 2003-2004 period. The displacement pattern obtained by applying the integration method are hence promising for future studies aimed at improving the knowledge on particular aspects of the dynamic of this volcano (e.g. the plumbing system, the flank dynamic, etc.).

The analysis of the accuracy, in terms of the estimated standard errors, highlight that it is in general lower than 4-5 mm, except for limited areas where the discrepancy between the original data is high probably due to local effects (e.g. time difference between GPS survey and SAR passes; high errors in GPS surveys, etc.). The analysis of the RMSE, for the case study of Mt Etna, allows to estimate the benefits which can be achieved by increasing the number of GPS points in the considered area. The detailed analysis on the RMSE confirms that SISTEM reinforces the Up component of the GPS data by effectively exploiting the DInSAR information. Widen this comment, we can state that the experiment on Mt. Etna confirms that SISTEM fully exploits the intrinsic complementarity of the DInSAR and GPS data for determining the ground deformations.

Among the potentiality of SISTEM we emphasize that, since it is based on the theory of the elasticity, we may include additional datasets (such as leveling data, EDM, Tilt, and DInSAR data taken from different geometry or by different SAR sensor, e.g. ENVISAT or ALOS), by

using similar formulations, based on the same unknowns. These potentialities will be fully exploited in future developments of the presented methods.

The great amount of data provided by the SISTEM method was successfully used in the framework of the inversion problem. In particular the seismic source associated to the 2009 Abruzzo earthquake was estimated by using a Particle Swarm Optimization algorithm. In this case study the potentiality of the SISTEM method to integrated different interferograms (ALOS, Envisat Ascending, Envisat Descending) was exploited.

Furthermore a method to investigate the volcanic source pressure shape using neural techniques was proposed. More specifically a neural network was opportunely trained in order to build, in the discrete Euclidian space, the shape source associated to a given 3D ground deformation pattern generated by several sources pressure. The most relevant result was the capability of generalization of the NN shown on both single and multi sources synthetic case studies. Indeed the NN trained by using patterns generated through single Mogi sources provided good results when used with multiple Mogi sources and with patterns generated by the ellipsoidal Davis model. The test performed on a real case study highlighted the suitability of the NN to detect source shape relevant to ground deformation pattern due to pressure source. However the NN was not able to suggest a source shape associated to the marked eastward movement of the eastern flank of the volcano. This was expected because such kinds of patterns are not due to sources pressure but they are relative to dislocation faults. This limit could be overcome by a new NN opportunely trained with specific pattern deformation due to dislocation sources. Otherwise future efforts could be also devoted to train a NN by using both pressure sources and dislocation faults in the attempt to recognize both kinds of source.

The proposed methodology could be a valid support in the framework of the inversion problem which are known to be nonunique. Indeed it provided a *a priori* information about

the geometric shape, for instance the volume, that could be successful used in order to acquire a reliable solution. Furthermore the output network could be processed by the Non-Uniform Rational B-Splines (NURBS) algorithm in order to provide a more reliable source shape that could be used in the framework of the Finite Element Modeling (FEM).

Appendix

A new method based on the Lagrange multipliers to reduce phase error affecting DInSAR data

Here a new method to reduce phase errors affecting the interferometric signals is shown. In particular, in a multi-interferogram framework, a mathematical optimization based on the method of Lagrange multipliers is used to reduce the phase contributions caused by the error in the DEM, the baseline and temporal decorrelation and the thermal noise effects. A preliminary synthetic test is provided.

Problem formulation

Let N be the number of SAR images relative of the investigated area and acquired at the ordered times $(t_1, t_2, \ldots, t_N)$. A generic interferogram φ_{ij} computed in the pixel of azimuth and range coordinates (x,r) from the SAR acquisitions at time t_i and t_j is given by

$$\varphi_{ij}(x,r) = \frac{4\pi}{\lambda}\left[d(t_j,x,r) - d(t_i,x,r)\right] + \left[\varphi_{atm}(t_j,x,r) - \varphi_{atm}(t_i,x,r)\right] + \varepsilon_{ij} + n_{ij} \qquad (1)$$

where λ is the system wavelength, $d(t_j,x,r)$ and $d(t_i,x,r)$ are the cumulative displacements in the direction of the Line Of Sight (LOS) at times t_j and t_i with respect to the instant t_0 assumed as a reference, $[\varphi_{atm}(t_j,x,r)-\varphi_{atm}(t_i,x,r)]$ is the atmospheric phase component, $\varepsilon_{ij} = \frac{4\pi}{\lambda}\frac{B_{ij}^{p}\Delta z}{r\sin\vartheta}$ is the phase contribution due to possible error Δz in the DEM (B_{ij}^{p} is the perpendicular baseline, r is the sensor target distance and θ is the look angle) and, finally, n_{ij} is the phase contribution caused by the baseline and temporal decorrelation and the thermal noise.

Starting from the following simple relations relative at each pixel *(x,r)* it is possible to define an optimization problem in order to reduce the phase contribution due to the terms ε_{ij} and n_{ij}:

$$\varphi_{12} + \varphi_{23} + \ldots + \varphi_{(N-1)N} - \varphi_{1N} = \varepsilon_{12} + \varepsilon_{23} + \ldots + \varepsilon_{(N-1)N} - \varepsilon_{1N} + n_{12} + n_{23} + \ldots + n_{(N-1)N} - n_{1N}$$

$$\varphi_{12} + \varphi_{23} + \ldots + \varphi_{(N-2)(N-1)} - \varphi_{1(N-1)} = \varepsilon_{12} + \varepsilon_{23} + \ldots + \varepsilon_{(N-2)(N-1)} - \varepsilon_{1(N-1)} + n_{12} + n_{23} + \ldots + n_{(N-2)(N-1)} - n_{1(N-1)}$$

$$\ldots\ldots$$

$$\varphi_{23} + \varphi_{34} + \ldots + \varphi_{(N-1)N} - \varphi_{2N} = \varepsilon_{23} + \varepsilon_{34} + \ldots + \varepsilon_{(N-1)N} - \varepsilon_{2N} + n_{23} + n_{34} + \ldots + n_{(N-1)N} - n_{2N}$$

$$\ldots\ldots$$

$$\varphi_{(N-2)(N-1)} + \varphi_{(N-1)N} - \varphi_{(N-2)N} = \varepsilon_{(N-2)(N-1)} + \varepsilon_{(N-1)N} - \varepsilon_{(N-2)N} + n_{(N-2)(N-1)} + n_{(N-1)N} - n_{(N-2)N}$$

(2)

Indeed the minimum of the multivariate function

$$f(\overline{\varphi}_{12}, \overline{\varphi}_{13}, \ldots, \overline{\varphi}_{(N-1)N}) = \sum_{i=1}^{N} \sum_{j=i+1}^{N} (\overline{\varphi}_{ij} - \varphi_{ij})^2 \qquad (3)$$

subject to the following constraints

$$\begin{aligned} & g_1 : \overline{\varphi}_{12} + \overline{\varphi}_{23} + \ldots + \overline{\varphi}_{(N-1)N} - \overline{\varphi}_{1N} = 0 \\ & g_2 : \overline{\varphi}_{12} + \overline{\varphi}_{23} + \ldots + \overline{\varphi}_{(N-2)(N-1)} = 0 \\ & \ldots \\ & g_k : \overline{\varphi}_{23} + \overline{\varphi}_{34} + \ldots + \overline{\varphi}_{(N-1)N} - \overline{\varphi}_{2N} = 0 \\ & \ldots \\ & g_M : \overline{\varphi}_{(N-2)(N-1)} + \overline{\varphi}_{(N-1)N} - \overline{\varphi}_{(N-2)N} = 0 \end{aligned} \qquad (4)$$

provides an estimate of the interferograms $\overline{\varphi}_{ij}$ for which the phase contributions due to the terms ε_{ij} and n_{ij} are strongly reduced.

This constraint optimization is suitably solved by the method of Lagrange multipliers. This method involves the introduction of so many variables λ_i, called the Lagrange multipliers, as there are constraints and the study of the Lagrange function defined by

$$\Lambda(\overline{\varphi}_{12},\overline{\varphi}_{13},...,\overline{\varphi}_{(N-1)N},\lambda_1,\lambda_2,...,\lambda_M) = f(\overline{\varphi}_{12},\overline{\varphi}_{13},...,\overline{\varphi}_{(N-1)N}) + \sum_{i=1}^{M}\lambda_i g_i(\overline{\varphi}_{12},\overline{\varphi}_{13},...,\overline{\varphi}_{(N-1)N}) \qquad (5)$$

A synthetic case study

The proposed methodology was tested on a synthetic dataset. For the sake of simplicity we have generated four acquisition scenes *(M_i, i=1..4)* by using different Mogi sources and calculated all the possible six interferograms according to $\varphi_{ij}(x,r) = M_j(x,r) - M_i(x,r) + ns$ (*i=1..4, j=2..3, j>i),* where *ns* is additive uniformly distributed white noise .

In figure 1 an example of the obtained results is reported. Two interesting advantages can be emphasized: 1) the optimized interferogram is smoother then the synthetic one; 2) the residual errors of the optimized interferogram exhibit a Gaussian distribution with zero mean. These performances clearly suggest the suitability of the proposed method to reduce noise affecting interferograms

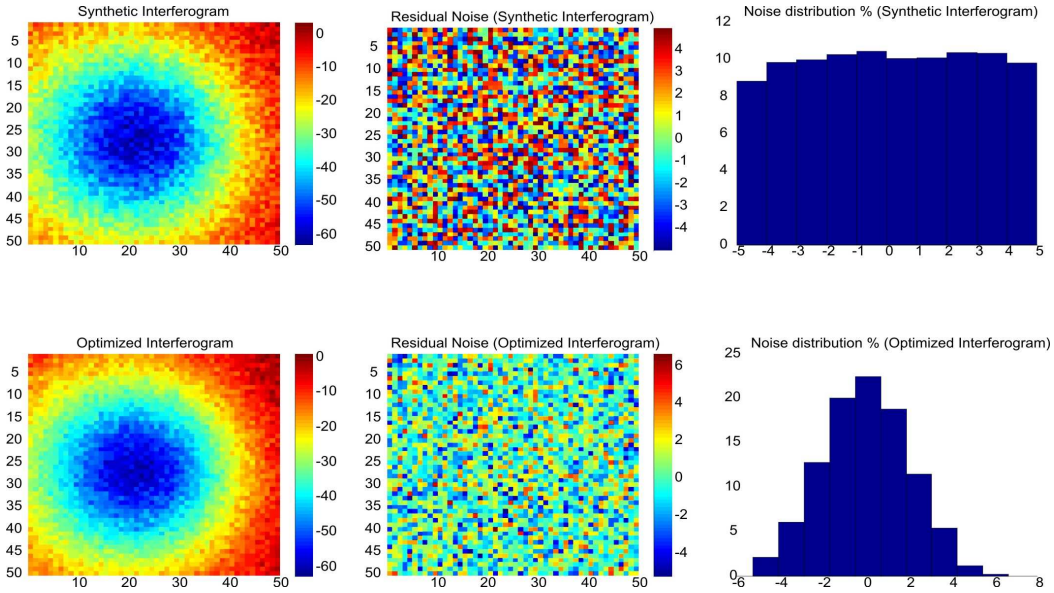

Figure 1. In the first row the initial synthetic interferogram, the noise added and the noise distribution are respectively reported. In the second row result after the application of the Lagrance multipliers based method are reported.

References

[1] Dzurisin, D., *Volcano deformation: geodetic monitoring techniques*. Berlin ; Heidelberg ; NewYork : Springer, 2007. - XXXV, pp. 441.

[2] Ding, X.L, Li, Z.W., Zhu J.J., Feng G.C, Long J.P., (2008), *Atmospheric Effects on InSAR Measurements and Their Mitigation*. Sensors, 8, 5426-5448; DOI: 10.3390/s8095426

[3] Bonforte, A., Ferretti, A., Prati, C., Puglisi, G., Rocca, F., (2001). *Calibration of atmospheric effects on SAR interferograms by GPS and local atmosphere models: first results*. J. Atmos. Sol.-Terr. Phys. 63, 1343–1357.

[4] Mattia, M., A. Bonaccorso, and F. Guglielmino (2007), *Ground deformations in the Island of Pantelleria (Italy): Insights into the dynamic of the current intereruptive period*, J. Geophys. Res., 112, B11406, doi:10.1029/2006JB004781.

[5] Chaabane, F.; Avallone, A.; Tupin, F.; Briole, P.; Maître, H., *A Multitemporal Method for Correction of Tropospheric Effects in Differential SAR Interferometry: Application to the Gulf of Corinth Earthquake*. IEEE T. Geosci. Remote Sens. 2007, 45, 1605-1615.

[6] Ding, X.-L.; Li, Z.-W.; Zhu, J.-J.; Feng, G.-C.; *Long, J.-P. Atmospheric Effects on InSAR Measurements and Their Mitigation*. Sensors 2008, *8*, 5426-5448.

[7] Hanssen, R.F. (2001) *Radar Interferometry: Data interpretation and Error Analysis*. Kluwer Academic Publishers: Dordrecht.

[8] Gudmundsson, S., F. Sigmundsson, and J. M. Carstensen (2002), *Three-dimensional surface motion maps estimated from combined interferometric synthetic aperture radar and GPS data*, J. Geophys. Res., 107(B10), 2250, doi:10.1029/2001JB000283.

[9] Samsonov, S. and Tiampo, K.F.(2006) *Analytical optimization of InSAR and GPS dataset for derivation of three-dimensional surface motion*, IEEE Geoscience and Remote Sensing Letters, 3/1, doi:10.1109/LGRS.2005.858483, pp. 107-111

[10] Knospe S., Jònsson S. (2007), *Covariance estimation for DInSAR deformation measurements in presence of strong atmospheric anisotropy*. Proceedings of the Envisat Symposium, Montreux, Switzerland (ESA SP-636, July 2007).

[11] Carstensen, J. M., *Description and simulation of visual texture*, Ph.D. thesis, Inst. for Math. Model., Tech. Univ. of Denmark, Lyngby, 1992.

[12] Li, S. Z., *Markov Random Field Modelling in Computer Vision*, Springer- Verlag, New York, 1995.

[13] Ross, S. M., *Introduction to Probability and Statistics for Engineers and Scientists*, John Wiley, New York, 1987.

[14] Besag, J., *Spatial interaction and the statistical analysis of lattice systems*, J. R. Stat. Soc., Ser. B, 36, 192–236, 1974.

[15] Geman, S., and D. Geman, *Stochastic relaxation, Gibbs distributions and the Bayesian restoration of images*, IEEE Trans. Pattern Anal. Mach. Intel., 6, 721–741, 1984.

[16] Williams, S., Y. Bock, and P. Fang, *Integrated satellite interferometry: Tropospheric noise, GPS estimates and implications for interferometric synthetic aperture radar products*, J. Geophys. Res., 103, 27,051– 27,067, 1998.

[17] Gudmundsson, S., *Crustal deformation mapped by combined GPS and InSAR*, M.Sc. thesis, Inst. for Math. Model., Tech. Univ. of Denmark, Lyngby, 2000.

[18] Nielsen, A. A., *Geostatistik og analyse af spatielle data*, report, Inst. For Math. Model., Tech. Univ. of Denmark, Lyngby, 1998.

[19] Vadon, H., and F. Sigmundsson, *Crustal deformation from 1992 to 1995 at the Mid-Atlantic Ridge, southwest Iceland, mapped by satellite radar interferometry*, Science, 275, 194– 197, 1997.

[20] Gudmundsson, S., M. T. Gudmundsson, H. Bjo¨rnsson, F. Sigmundsson, H. Rott, and J. M. Carstensen, *Three-dimensional glacier surface motion maps at the Gja´lp eruption site*, Iceland, inferred from combined InSAR and other ice displacement data, Ann. Glaciol., 34, 315– 322, 2002b.

[21] P. Brooker, *A Geostatistical Primer*. Singapore: World Scientific, 1991.

[22] C. Deutsch and A. Journel, *GSLIB Geostatistical Software Library and User's Guide*. Oxford, U.K.: Oxford Univ. Press, 1992.

[23] F. Guglielmino, G. Nunnari, G. Puglisi, A. Spata, *Simultaneous and Integrated Strain Tensor Estimation from geodetic and satellite deformation Measurements (SISTEM) to obtain three-dimensional displacement maps*, submitte to IEEE Geoscience and Remote Sensing

[24] Teza,G.,Pesci,A., Galgaro,A.,(2008) *Grid_strain and grid_strain3: Software packages for strain field computation in 2D and 3D environments*, Computers & Geosciences, Volume 34, Issue 9, September 2008, Pages 1142-1153, ISSN 0098-3004, DOI: 10.1016/j.cageo.2007.07.006.

[25] Pietrantonio, G. and Riguzzi, F., (2004) *Three-dimensional strain tensor estimation by GPS observations: methodological aspects and geophysical applications*. Journal of Geodynamics 38, (2004),1-118 doi:10.1016/j.jog.2004.02.021

[25] Shen, Z.-K., Jackson, D.D., and B.X. Ge (1996). *Crustal deformation across and beyond the Los Angeles basin from geodetic measurements*, Journal of Geophysical Research 101, pp. 27957–27980

[26] Pesci, A. and G. Teza, (2007). *Strain rate analysis over the central Apennines from GPS velocities: the development of new free software*. Bollettino di Geodesia e Scienze Affini. v56. 69-88.

[27] E. LIVIERATOS, 1980: *Crustal deformations from geodetic measurements*.Bollettino di Geofisica Teorica ed Applicata, Vol. 22, No. 88, 255–260.

[28] Frank, F.C., (1966). *Deductions of earth strains from survey data*. Bull. Seismol. Soc. Am. 56 1, pp. 35–42.

[29] Prescott, W. H. (1976). *An extension of Frank's method for obtaining crustal shear strains from survey data*, Bull. Seismol. Soc. Am., 6+6, 1847-1853.

[30] Chiles, J.P., P. Delfiner, 1999, *Geostatististics, Modelling Spatial Uncertainty*, Wiley-Interscience

[31] Sudhaus, H., and S. Jónsson, *Improved source modeling through combined use of InSAR and GPS under consideration of correlated data errors: Application to the June 2000 Kleifarvatn earthquake Iceland*, Geophys. J. Int., 176, 389-404, 2009.

[32] Williams C.A. and G. Wadge (1998), *The effects of topography on magma deformation models: application to Mt. Etna and radar interferometry*. Geophys. Res. Lett. 25 (1998), pp. 1549–1552.

[33] Lohman, R. B., and M. Simons (2005), *Some thoughts on the use of InSAR data to constrain models of surface deformation: Noise structure and data downsampling*, Geochem. Geophys. Geosyst., 6, Q01007, doi:10.1029/2004GC000841.

[34] Mogi, K. (1958) *Relation between the eruptions of various volcanoes and the deformation of ground surfaces around them*, Bulletin of the Earthquake Research Institute, Tokyo University 36 (1958), pp. 99–134.

[35] Williams, C. A., and Wadge (2000), *An accurate and efficient method for including the effects of topography in three-dimensional elastic models of ground deformation with applications to radar interferometry*, J. Geophys. Res., 105(B4)

[36] HE XiuFeng, LUO HaiBin, HUANG QiHuan and HE Min (2007), *Integration of InSAR and GPS for hydraulic engineering*, Journal Science in China Series E: Technological Sciences Publisher Science in China Press, co-published with Springer-Verlag GmbH ISSN 1006-9321 (Print) 1862-281X (Online) Issue Volume 50, Supplement 1 / October, 2007 DOI 10.1007/s11431-007-6009-3 Pages 111-124 Subject Collection Engineering SpringerLink Date Saturday, November 10, 2007

[37] Vaníček, P., Grafarend, E.; Berber, M.(2008), *Short Note: Strain invariants*. Journal of Geodesy, Volume 82, Numbers 4-5, April 2008 , pp. 263-268(6) doi:10.1007/s00190-007-0175-8

[38] Samsonov, S., Tiampo, K.F. Rundel J., Li Z. (2007) *Application of DInSAR - GPS optimization for derivation of fine-scale surface motion maps od Southern California*, IEEE Transaction on Geoscience and Remote Sensing, 45/2, doi:10.1109/TGRS.2006.887166, pp. 512-521.

[39] A. Bonaccorso, , A. Bonforte, F. Guglielmino, M. Palano, and G. Puglisi (2006), *Composite ground deformation pattern forerunning the 2004–2005 Mount Etna eruption*, J. Geophys. Res., 111, B12207, doi:10.1029/2005JB004206.

[40] Bonforte, A., A. Bonaccorso, F. Guglielmino, M. Palano, and G. Puglisi (2008), *Feeding system and magma storage beneath Mt. Etna as revealed by recent inflation/deflation cycles*, J. Geophys. Res., 113, B05406, doi:10.1029/2007JB005334.

[41] Palano M., Puglisi G., Gresta S., (2008). *Ground deformation patterns at Mt. Etna from 1993 to 2000 from joint use of InSAR and GPS techniques*. Journal of Volcanology and Geothermal Research 169, 99–120.

[42] J. Kennedy and R. Eberhart, *Particle Swarm Optimization*, in Proc. IEEE int. Conf. Neural Network, vol. IV, 1995, pp. 1941-1948

[43] Clerc M., Kennedy J. (2002). *The Particle Swarm: explosion, stability and convergence in a multi-dimensional complex space*. IEEE Trans Evol Comput 6:58-73.

[44] Eberhart R.C., Shi Y., (2000), *Comparing Inertia Weigths and Constriction Factor in Particle Swarm Optimization*. In: Proceedings of the IEEE congress evolutionary computation, San Diego, CA, pp 84-88

[45] Parsopoulus, K.E., Vrahatis, M.N. (2002). *Recent Approaches to Global Optimization Problems through Particle Swarm Optimization*. Natural Computing 1 (2-3), pp. 235-306.

[46] Okada, Y, (1985), *Surface deformation due to a shear and tensile faults in a halfspace.* Bull. Seismol. Soc. Amer., vol. 75, pp. 1135-1154

[47] M. Poulton, B. K. Sternberg and C. E. Glass, (1992) *Neural network pattern recognition of subsurface EM image*, Journal of Applied Geophysics, Volume 29, Issue 1

[48] G. Roth, A. Tarantola (1992), *Inversion of seismic waveform using neural networks.* 62nd SEG meeting, New Orleans, USA, Expanded Abstract

[49] C. Calderon-Macias, M. K. Sen, P. L. Stoffa (2000), *Artificial Neural networks for parameter estimation in geophysics*, Geophysical Prospecting, Volume 48, Issue 1,

[50] Nunnari, G., Bertucco, L., Ferrucci, F., (2001) *A neural approach to the integrated inversion of geophisical data types,IEEE Transaction on Geoscience and Remote Sensing, vol 39, n. 4*

[51] P. J.Werbos, *Beyond regression: New tools for prediction and analysis in behavioral sciences*, M.A. Thesis, Harvard Univ., Cambridge, MA, 1974.

[52] D. E. Rummelhart, G. E. Hinton, and R. J. Williams, *Learning internal representation by error propagation*, in Parallel Distributed Processing. Cambridge, MA: MIT Press, 1986, vol. 1, pp. 318–362.

[53] J. A. Freeman and D. M. Skapura, *Neural Networks—Algorithms, Applications and Programming Techniques*. Reading, MA: Addison- Wesley, 1992.

[54] G. Cybenko, *Approximation by super precision of a sigmoidal function*, in Math of Control Signals and Systems. New York: Springer- Verlag, 1989, vol. 2, pp. 303–314.

[55] M. K. Sen and P. L. Stoffa, "Nonlinear one-dimensional seismic waveform inversion using simulated annealing," *Geophysics*, pp. 1624–1638, 1991.

[56] F. Scherbaum, C. Palme, and H. Langer, *Model parameter optimization for site dependent simulation of ground motion by simulated annealing: Reevaluation of the Ashigara Valley prediction experiment*, Natural Hazards, vol. 10, pp. 275–296, 1994.

[57] McTigue, D.F., (1987). *Elastic stress and deformation near a finite spherical magma body: resolution of the point source paradox,* Journal of Geophysical Research, vol. 92, no. B12, PP. 12,931-12,940

[58] Davis, P.M., 1986. *Surface deformation due to inflation of an arbitrarily oriented triaxial ellipsoidal cavity in an elastic half-space, with reference to Kilauea Volcano*, Hawaii, J. geophys. Res., 91, 7429–7438.